

1 **Reactivation of intrabasement structures during rifting: A case study from**
2 **offshore Norway**

3 **Thomas B. Phillips**^{1*}, **Christopher A-L. Jackson**¹, **Rebecca E. Bell**¹, **Oliver B. Duffy**²,
4 **Haakon Fossen**³

5 ***Corresponding author: t.phillips13@imperial.ac.uk**

6 ¹ *Basins Research Group (BRG), Department of Earth Science and Engineering, Imperial*
7 *College, South Kensington Campus, Prince Consort Road, London, SW7 2BP, UK*

8 ² *Bureau of Economic Geology, Jackson School of Geosciences, The University of Texas at*
9 *Austin, University Station, Box X, Austin, TX 78713-8924, USA*

10 ³ *Department of Earth Science/Natural History Collections, University of Bergen, Allégaten*
11 *41, 5008 Bergen, Norway*

12 **Abstract**

13 Pre-existing structures within crystalline basement may exert a significant influence over the
14 evolution of rifts. However, the exact manner in which these structures reactivate and thus
15 their degree of influence over the overlying rift is poorly understood. Using borehole-
16 constrained 2D and 3D seismic reflection data from offshore Southern Norway we identify
17 and constrain the three-dimensional geometry of a series of enigmatic intrabasement
18 reflections. Through 1D waveform modelling and 3D mapping of these reflection packages,
19 we correlate them to the onshore Caledonian thrust belt and Devonian shear zones. Based on
20 the seismic-stratigraphic architecture of the post-basement succession we identify several
21 phases of reactivation of the intrabasement structures associated with multiple tectonic
22 events. Reactivation preferentially occurs along relatively thick (c. 1km), relatively steeply

23 dipping (c. 30°) structures, with three main styles of interactions observed between them and
24 overlying faults: (i) faults exploiting intrabasement weaknesses represented by intra-shear
25 zone mylonites; (ii) faults that initiate within the hangingwall of the shear zones, inheriting
26 their orientation and merging with said structure at depth; or (iii) faults that initiate
27 independently from and cross-cut intrabasement structures. We demonstrate that large-scale
28 discrete shear zones act as a long-lived structural template for fault initiation during multiple
29 phases of rifting.

30 **1. Introduction**

31 Continental rifting is often considered in terms of extension of relatively homogeneous
32 lithosphere (Gupta et al., 1998; Cowie et al., 2000; Gawthorpe and Leeder, 2000). However,
33 continental lithosphere is considerably more complex than envisaged in these idealised
34 models, typically containing a range of structures imparted by previous tectonic events. These
35 structures span a range of scales; from large-scale crustal sutures and orogenic belts (Daly et
36 al., 1989; Mogensen and Korstgård, 2003; Paton and Underhill, 2004; Bird et al., 2014;
37 Bladon et al., 2015), pre-existing fault populations and outcrop-scale fault and fracture
38 networks (Kirkpatrick et al., 2013; Whipp et al., 2014; Duffy et al., 2015), to structures
39 formed at the grain- and even micro-scale. Such pre-existing heterogeneities may; i)
40 reactivate during later tectonic events; ii) act as nucleation sites for later rift-related faults;
41 and iii) localise and modify the regional stress field, thus fundamentally modifying the
42 physiography and evolution of overlying rifts. Field, seismic and potential field data indicate
43 that the reactivation of intrabasement structures may influence the development of rift
44 systems (Daly et al., 1989; Fraser and Gawthorpe, 1990; Maurin and Guiraud, 1993; Ring,
45 1994; Færseth, 1996; Clemson et al., 1997; Morley et al., 2004; Paton and Underhill, 2004;
46 Gontijo-Pascutti et al., 2010; Bellahsen et al., 2013; Bird et al., 2014; Whipp et al., 2014;
47 Salomon et al., 2015; Scheiber et al., 2015), an observation further supported by numerical

48 and analogue modelling (Huyghe and Mugnier, 1992; Faccenna et al., 1995; Bellahsen and
49 Daniel, 2005; Henza et al., 2011; Autin et al., 2013; Chattopadhyay and Chakra, 2013; Tong
50 et al., 2014). However, many of these relationships between intrabasement structure and rift
51 systems are simply based on plan-view correlations, with little consideration given to their
52 three-dimensional geometric relationships or kinematic interactions, primarily due to
53 difficulties in imaging and constraining the 3D geometry of the intrabasement structure. For
54 instance, in seismic reflection data, crystalline basement often appears acoustically
55 transparent due to typically low internal impedance contrasts and large burial depths.

56 Although intrabasement structures have previously been imaged using deep seismic reflection
57 data (Chadwick et al., 1983; Choukroune, 1989; Abramovitz and Thybo, 2000; Hedin et al.,
58 2012; Fossen et al., 2014), these studies have sparse data coverage and are unable to resolve
59 the required detail and 3D geometry of said structures, particularly at upper crustal levels. In
60 addition, interpretations based upon potential field data may be non-unique and of relatively
61 low resolution, with these data typically unable to image discrete structures. In contrast,
62 discrete structures can be analysed in some detail in the field, although these data may not be
63 of sufficient extent to permit truly three-dimensional analysis of large-scale structure.

64 Recent advances in the quality of seismic data have allowed for the detailed mapping of
65 intrabasement structures on both 2D (Bird et al., 2014) and 3D (Reeve et al., 2013; Bird et al.,
66 2014) seismic reflection data, and it has been demonstrated that these structures can both
67 influence (Bird et al., 2014) or not influence (Reeve et al., 2013) the structural style and
68 evolution of later rift systems. Therefore, the selective reactivation of intrabasement
69 structures may depend on physical and geometric properties related to their formation and
70 composition, as well as their relation to regional stress fields imposed during later tectonic
71 events. A detailed understanding of the overall 3D geometry and internal architecture of

72 intrabasement structures is therefore vital to determine the controls on their selective
73 reactivation and how this affects the geometry and evolution of the overlying rift.

74 In this study we use closely spaced 2D and 3D seismic reflection data from offshore SW
75 Norway (Figure 1, 2) to constrain the 3D geometry of a series of enigmatic reflection
76 packages within crystalline basement, along with key stratigraphic horizons in the overlying
77 rift. Being located close to the margin of the North Sea rift basin and having experienced a
78 complex tectonic history (Figure 3), crystalline basement in the study area is located at
79 relatively shallow depths (<4.5 km) and is highly heterogeneous, containing a series of
80 prominent coherent reflections that can be mapped across large parts of the seismic data. We
81 observe two types of discrete reflection packages within crystalline basement: i) thin (c. 100
82 m) reflection packets displaying a concave-upwards geometry (Figure 4); and ii) thicker (c.
83 1.5 km) reflection packages of inclined reflectivity that dip at c. 30° (Figure 4). Through 1D
84 waveform modelling, we show that these reflections originate from a layered sequence,
85 which we propose are layered intra-shear zone mylonites. Furthermore, because the study
86 area is located close to the Norwegian coastline (Figure 1), we are able to confidently link
87 these reflections to the previously mapped and established onshore geology, specifically
88 shear zones associated with the Caledonian Orogeny and the Devonian orogenic collapse
89 (Morley, 1986; Pedersen and Hertogen, 1990; Fossen and Rykkelid, 1992; Gabrielsen et al.,
90 2002; Fossen, 2010; Roffeis and Corfu, 2013; Corfu et al., 2014).

91 Based upon our seismic interpretation of both the cover and the basement, we observe a range
92 of interactions between the intrabasement structures and the overlying rift-related faults
93 throughout multiple tectonic events. In some instances reactivation of intrabasement
94 structures has a profound effect on the later rift; whereas in others, rift-related faults form
95 independently of intrabasement structure. As such, we investigate the factors controlling this

96 selective reactivation of the intrabasement structures and offer insights into the mechanisms
97 of their reactivation.

98 **2. Geological Setting**

99 **2.1 Regional setting**

100 This study focuses on a 20,000 km² area located offshore SW Norway, encompassing the
101 WNW- trending Egersund Basin, the N-trending Åsta Graben (Figure 1), and the Stavanger
102 Platform (Figure 1). The major basement-involved faults in the study area are the Åsta Fault,
103 and the Stavanger and Sele High Fault Systems, bounding the Åsta Graben, Stavanger
104 Platform and Sele High respectively (Figure 1). The Stavanger Fault System (SFS) consists
105 of two NW-to-NNW striking fault segments (Figure 1). The Åsta fault strikes N-S along the
106 eastern margin of the Åsta Graben. Between the Åsta and Stavanger fault systems, the south-
107 western margin of the Stavanger Platform is bordered by a shallowly dipping ramp, herein
108 termed the Stavanger Ramp (Figure 1). The N-S striking Sele High Fault System (SHFS)
109 forms the western boundary to the Åsta Graben and the Egersund Basin (Figure 1).

110 **2.2 Geological History**

111 The present day crystalline basement of the North Sea largely formed during the Late
112 Ordovician-Early Devonian Caledonian orogeny (McKerrow et al., 2000) (Figure 3), with
113 older Proterozoic basement remnant to the east of the study area. The Scandian phase of the
114 Caledonian orogeny involved continent-continent collision between Laurentia to the west and
115 Baltica in the east. During this collision, allochthonous material was transported ESE onto the
116 margin of Baltica along a basal zone of mechanically weak Cambrian shales and phyllites
117 overlain by a package of highly sheared rocks of Baltican origin, collectively referred to as
118 the basal décollement zone (Figure 1) (Fossen, 1992; Milnes et al., 1997). The Caledonian

119 Deformation Front (CDF) represents the easternmost limit of Caledonian allocthonous
120 material. The in-situ CDF is preserved along eastern Norway, whereas post Caledonian
121 erosion across large parts of southern Norway results in the westward translation of the CDF
122 as observed today (Huuse, 2002; Japsen et al., 2002). Hence, the original CDF can only
123 approximately be located in the area covered by Figure 1. In this study, we refer to the CDF
124 as the present, erosional boundary between Caledonian allochthonous material and
125 Proterozoic autochthonous crystalline basement (Figure 1).

126 Caledonian shortening was succeeded by Devonian orogen-scale extension (McClay et al.,
127 1986; Dewey, 1988; Fossen, 1992)(Figure 3). Extension was initially accommodated by the
128 reactivation of pre-existing Caledonian structures (Mode I reactivation of Fossen et al.,
129 1992), most notably the basal décollement, as indicated onshore by asymmetric mylonitic
130 fabrics and the overprinting of top-to-SE by top-to-NW shear sense indicators (Fossen, 1992).
131 This reversal of shear along Caledonian structures accounted for 20-30 km of extension
132 across Norway before these structures became locked at low angles. Subsequent extension
133 was accommodated by the formation of large-scale through-going extensional shear zones
134 (Mode II reactivation of Fossen et al., 1992) and a series of Devonian basins (Fossen, 2010;
135 Vetti and Fossen, 2012). The extensional shear zones are mapped onshore across southern
136 Norway to the northern margin of the study area along the present coastline (Pedersen and
137 Hertogen, 1990; Fossen, 2010; Bøe et al., 2011). These shear zones are typically 1-2 km
138 thick, with some up to 5 km (Fossen and Hurich, 2005).

139 Extension in the Carboniferous-Early Permian, potentially in response to post-Variscan
140 orogenic collapse (Ziegler, 1992), resulted in the formation of a number of major faults,
141 notably the Sele High and Stavanger fault systems (Sørensen et al., 1992; Jackson and
142 Lewis, 2013; Jackson and Lewis, 2015) (Figure 1). Subsequent post-rift thermal subsidence
143 led to the formation of the North and South Permian basins, which, during the Late Permian

144 were filled with the evaporite-dominated Zechstein Supergroup (Ziegler, 1992). During the
145 Mesozoic, the North Sea experienced two main rift phases, the first occurring during the Late
146 Permian-Early Triassic in response to the breakup of Pangea. E-W-directed extension
147 (Coward et al., 2003; Fossen et al., 2016) led to the development of a predominately N-
148 trending rift (Ziegler, 1992; Odinsen et al., 2000), the formation of the Åsta fault, and the
149 reactivation of other major faults within the study area (Sørensen et al., 1992; Jackson and
150 Lewis, 2013; Jackson and Lewis, 2015). A second rift phase lasted from the Late Jurassic into
151 the Early Cretaceous, with previous studies suggesting an extension direction of either E-W
152 (Bartholomew et al., 1993; Brun and Tron, 1993; Bell et al., 2014) or WNW-ESE to NW-SE
153 (Færseth, 1996; Doré et al., 1997; Færseth et al., 1997). Rifting resulted in the initiation of
154 new faults and the reactivation of some pre-existing faults (Bell et al., 2014), including a
155 number of those located within the study area (Figure 3). This rift phase occurred in response
156 to the collapse of a Middle Jurassic Mid-North Sea Dome (Underhill and Partington, 1993),
157 which broadly coincided with the opening of the Norwegian Sea - North Atlantic rift system
158 (Ziegler, 1992). Following Late Jurassic-to-Early Cretaceous rifting, a protracted period of
159 post-rift thermal subsidence was interrupted during the Late Cretaceous by mild inversion
160 related to the Alpine orogeny (Figure 3) (Biddle and Rudolph, 1988; Cartwright, 1989;
161 Jackson et al., 2013).

162 **3. Dataset and methodology**

163 Key horizons and structures were mapped on a closely spaced (maximum 5 km spacing) grid
164 of 2D seismic reflection data (imaging to 7-9 s two-way-travel time, TWT), and a 3600 km²
165 3D dataset with 25 m line spacing (imaging to 5 s TWT) (Figure 2). Seismic reflection data
166 are zero-phase and displayed following the SEG reverse polarity convention; i.e. a downward
167 increase in acoustic impedance is represented by a trough (red) and a downward decrease in
168 acoustic impedance is represented by a peak (black) (Figure 5). The ages of key seismic

169 horizons were constrained using 17 boreholes, three of which penetrate crystalline basement
170 (Figure 3). Checkshot data from these wells were used to create a velocity model to convert
171 structural measurements from the time to depth domain.

172 The dominant intrabasement frequency within the 2D seismic data is c. 20 Hz; using an
173 interval velocity of 6100 ms^{-1} for crystalline basement (Abramovitz and Thybo, 2000), we
174 estimate an intrabasement vertical resolution of c. 80 m. The quality of imaging within
175 basement is generally very good, although it deteriorates towards the SE due to thicker
176 Zechstein salt in the eastern Egersund Basin. Intrabasement reflections were mapped, where
177 possible, within the 3D volume and across individual closely spaced 2D lines. The distinct
178 seismic expression of the larger intrabasement features (Figure 5, 6) allowed for correlation
179 between individual 2D lines, allowing them to be mapped over a larger area and to greater
180 depths than permitted by the 3D volume alone (Figure 3).

181 Seismic-scale variations in crystalline basement lithology typically produce small impedance
182 contrasts, due to minor differences in seismic velocity and density, and do not produce
183 prominent reflections in seismic reflection data. Therefore, in conjunction with the typically
184 large burial depths of crystalline basement beneath rifts, intrabasement structures are often
185 poorly resolved on seismic reflection data (Torvela et al., 2013). However, imaging of
186 crystalline basement may be improved within areas of shallow basement. In addition,
187 intrabasement reflectivity may be enhanced through constructive interference within layered
188 sequences, such as those observed between highly strained mylonite zones and less deformed
189 country rock (Fountain et al., 1984; Wang et al., 1989).

190 1D waveform modelling was used to test the geological origin of the characteristic reflection
191 patterns observed within the intrabasement structures. We make no attempt to model the
192 absolute or relative amplitudes of the data, instead focussing on the interference between

193 reflections and the first-order reflection patterns. In addition, we do not account for
194 attenuation of the seismic wave with depth. Reflection co-efficients of +1 and -1 were
195 assumed for increases and decreases in acoustic impedance respectively. Taking into account
196 the reverse data polarity, we use an incident negative ricker wavelet of 20 Hz, assuming an
197 intrabasement velocity of 6100 ms^{-1} . Wavelet responses were calculated from horizons at
198 varying depths and then convolved to produce the overall model reflection pattern.

199

200 **4. Interpretation of intrabasement structure**

201 **4.1 Offshore intrabasement reflectivity**

202 We observe two types of prominent reflections within crystalline basement: i) relatively thin
203 (c. 80-100 m), concave-upwards, high-amplitude reflection packets that dip $0-10^\circ$ and are
204 characterised by a trough-peak-trough wavetrain (Figure 4a); and ii) relatively thick (c. 1-2
205 km) packages of high-amplitude reflectivity dipping at c. 30° , which are herein termed
206 intrabasement packages (IP) (Figure 4a). In detail, the IP comprise an anastomosing network
207 of high-amplitude, sub-parallel reflections (Figure 4a, 5). Although the overall geometry of
208 the IP, i.e. the top and base of the packages, can be mapped across multiple 2D seismic
209 sections (Figure 6, 7), we are unable to map individual internal reflections as they are often
210 laterally discontinuous (Figure 6).

211 Basement-penetrating wells (Figure 2) sample Caledonian and Proterozoic crystalline
212 basement, confirming that the mapped deep reflectivity is within crystalline basement. The
213 geometry and extent of the reflections do not mimic that of any reflections in the overlying
214 cover, thus we argue they are not multiples (Figure 5). Furthermore, the intrabasement

215 reflections are visible across independent seismic datasets, suggesting that they represent real
216 geological boundaries rather than an acquisition- or processing-related geophysical artefact.

217 **4.2 Waveform modelling of intrabasement reflections**

218 Later in this paper, we correlate the large scale intrabasement packages described above to
219 discrete basement shear zones that are mapped onshore southern Norway. However, we first
220 here use 1D waveform modelling to demonstrate that the observed reflection patterns
221 resemble the general internal geometries of shear zones described elsewhere.

222 1D waveform modelling allows us to recreate first-order reflection patterns observed in the
223 data. First, we find that the observed first-order reflection pattern, the characteristic trough-
224 peak-trough wavetrain, cannot be generated using a single interface, instead forming through
225 constructive interference between reflections generated within a layered sequence (Figure
226 4b). We therefore produce a series of layered models with different layer and interlayer
227 thicknesses (Fountain et al., 1984) and compare these to the observed reflection patterns
228 (Figure 4b). A reflection coefficient of -1 was used to define the top of a layer, and +1 used to
229 define the base (Figure 4b).

230 Our analyses show that reflections produced by closely spaced (c. 100 m) layers
231 constructively interfere to create a trough-peak-trough wavetrain, similar to the thin reflection
232 packets observed within the data (Figure 4a,b). We find that the observed intrabasement
233 reflection patterns are best represented by c. 100 m thick layers of material with a lower
234 acoustic impedance (AI) separated by 50-100 m of higher acoustic impedance material. In the
235 example shown in Figure 4b, 100 m thick low-AI layers, separated by 50 m thick, high-AI
236 layers best fit the upper segment of the observed reflection pattern, whereas a high-AI layer
237 thickness of 100 m best fits the lower part. Furthermore, we find that continually adding
238 similarly spaced layers to the sequence acts to increase the number of cycles present in, and

239 therefore the overall thickness of, the overall reflection package, resembling the observed IPs
240 (Figure 4a,b). As the spacing between layers increases, the degree of constructive
241 interference decreases until two distinct reflections can be resolved. At a spacing of >150 m,
242 layers begin to produce two distinct reflection events (Figure 4b), as opposed to
243 constructively interfering within one another. Slight variations in layer and interlayer
244 thicknesses result in differing degrees of interference, causing variations in the imaging of
245 individual layered sequences. Prominent reflections within the package may represent areas
246 displaying the optimal spacing (c. 50-100 m) for constructive interference, with less distinct
247 reflections generated at non-optimal layer and interlayer thicknesses.

248 Based on our modelling results we propose that the observed intrabasement structures most
249 likely represent intra-shear zone mylonites. Previous studies have also correlated similar
250 structures observed in seismic reflection data, showing the characteristic trough-peak-trough
251 wavetrain, to mylonite zones as observed onshore (Fountain et al., 1984; Hurich et al., 1985;
252 Reeve et al., 2013), with some offering direct control through outcrop and well data (Wang et
253 al., 1989; Hedin et al., 2012; Lorenz et al., 2015). In addition, our observed thicknesses of c.
254 100 m are of a similar scale to those proposed in previous modelling studies (Fountain et al.,
255 1984; Reeve et al., 2013), and the internal structure of these intra-shear zone mylonites
256 display a similar anastomosing geometry to those observed elsewhere; for example, onshore
257 Norway (Boundy et al., 1992; Scheiber et al., 2015), the central alps (Choukroune and
258 Gapais, 1983), the Cap de Creus shear zone network (Druguet et al., 1997; Carreras, 2001;
259 Carreras et al., 2010; Ponce et al., 2013) and southern Africa (Goscombe et al., 2003;
260 Goscombe and Gray, 2008; Rennie et al., 2013). However, we must also consider that the
261 observed 100 m scale mylonites only reflect one scale of localisation present within shear
262 zones (Carreras, 2001); the top and base of thicker mylonite zones may not constructively
263 interfere and produce a prominent seismic reflection, whereas thinner mylonite zones may

264 not be resolved in our seismic data. The modelled mylonite zones may actually represent a
265 high concentration of thinner mylonite layers, at thicknesses below seismic resolution and
266 therefore producing the same reflection pattern as a thicker mylonite zone (Carreras, 2001).

267 **4.3 Geometry of offshore intrabasement structures**

268 Having modelled the reflection patterns within the intrabasement reflection packages and
269 having argued that these may be linked to intra-shear zone mylonites (Figure 4b), we now
270 provide a more detailed description of the overall geometry of the discrete reflection
271 packages in order to link them explicitly to specific basement structures mapped onshore. A
272 series of thin reflection packets are observed above a shallowly dipping intrabasement
273 package, termed IP1 (Figure 5, 6). IP1 in turn is cross-cut by other intrabasement packages,
274 termed IP2 and IP3 (Figure 5). A further intrabasement package, IP4 is observed further to
275 the south (Figure 6, 7). We now describe the 3D geometry of these intrabasement packages.

276 IP1 is 0.5-1 s TWT (c. 1 km) thick and is the lowermost intrabasement package mappable
277 within the study area. IP1 predominately dips 0° to 11° W, although it may locally dip
278 shallowly to the east, and is truncated by the top basement unconformity beneath the
279 Stavanger Platform (Figure 5, 6). To the north of the study area, beneath the Stavanger
280 Platform, IP1 is cross-cut by intrabasement structures IP2 and IP3 (Figure 5). IP1 is not
281 visible to the west and in the hanging wall of IP2. To the south, IP1 is mapped beneath the
282 Egersund Basin and Flekkefjord High (Figure 1), within the hanging wall of the Sele High
283 Fault System, where it is slightly offset by IP4 (Figure 7, 8). Across the Stavanger platform, a
284 series of relatively thin (100 ms or c. 100 m) reflection packets are locally mapped (over c.
285 750 km^2 ; Figure 9). These reflections sole-out onto IP1, strike N-S and dip westwards at 0-
286 10° , displaying a concave-upwards geometry. When viewed collectively they exhibit a flat-
287 ramp style geometry (Figure 6).

288 IP2 is 1-1.5s TWT (c. 2 km) thick. Along the western margin of the Stavanger Platform it is
289 truncated along the top basement unconformity, where it strikes N-S and dips c. 30° W
290 (Figure 5). Here, IP1 is present in the footwall but not the hangingwall of IP2. Further south,
291 beneath the Stavanger ramp and Egersund Basin, IP2 strikes NE-SW before being offset by c.
292 2 s TWT by the N-S striking Sele High Fault System (Figure 9). Along the northern part of
293 the Sele High Fault System, IP2 is truncated by the top basement unconformity in the
294 hanging wall of the fault; whereas in the centre it is offset and is present on both sides of the
295 fault, and in the south it is only present within the footwall (Figure 8). In the south, where IP2
296 is only present in the footwall of the Sele High Fault System, IP1 is not offset, and is present
297 within the hanging wall of IP2 and the hanging wall of the Sele High Fault System.

298 IP3 is 1-1.5 s TWT (c. 2 km) thick and is truncated at the top basement unconformity across
299 the Stavanger Platform (Figure 5). IP3 strikes roughly N-S, dips c. 30° W, and also offsets
300 IP1 (Figure 5). A local basin, herein termed the Stavanger Basin, is present above the
301 structure (Figure 5). Limited data coverage across the Stavanger Platform does not allow for
302 detailed mapping of the package, although it is observed along strike further to the south
303 along the southern margin of the Stavanger Platform and the Stavanger Fault System (Figure
304 7).

305 A further intrabasement structure, IP4, splays-off southwards from IP2, beneath the Egersund
306 Basin and Flekkefjord High. This IP is 0.5-1 s (0.5-1 km) thick, strikes 010° N and dips 30°
307 W (Figure 6, 7, 8). IP4 also offsets IP1 and may merge with IP2 at depth (Figure 6) and along
308 strike to the north (Figure 9). East of IP4, several other IPs are observed in, and possibly
309 splay off from, the hanging wall of the larger structure (Figure 8). These may represent
310 additional IPs splaying from IP4, mirroring the geometric relationship of IP2 and IP4 further
311 to the north (Figure 7); or alternatively, a segment of IP1 within the footwall of IP4.

312 **4.5. Onshore-offshore correlation of intrabasement structures**

313 Based on our waveform modelling showing that the intrabasement reflections represent intra-
314 shear zone mylonites (Figure 4), and combined with their overall 3D geometry, we now link
315 our offshore intrabasement structures to specific shear zones mapped onshore. In particular,
316 we link them to the CDF and Devonian extensional shear zones that have previously been
317 studied and mapped in great detail (Figure 1) (Fossen, 1992; Fossen and Dunlap, 1998;
318 Gabrielsen et al., 2002; Olesen et al., 2004; Bingen et al., 2008; Bøe et al., 2011; Lundmark
319 et al., 2013; Roffeis and Corfu, 2013).

320 The subcrop of IP1 at top crystalline basement correlates along strike northwards to the CDF
321 onshore. In addition, basement-penetrating wells (18/11-1; Figure 9) sample Caledonian
322 crystalline basement (Sørensen et al., 1992) west of IP1, and a Proterozoic granite to the east
323 (10/5-1; Figure 9), indicating that the CDF must lie between these locations (Figure 9). Based
324 on our seismic mapping of IP1, and supported by these observations and the 1D waveform
325 modelling, we interpret IP1 to represent the offshore continuation of the basal décollement
326 zone of the Caledonian thrust belt, with the subcrop at top basement level representing the
327 CDF itself. To the south, our interpretation of the CDF correlates along strike to the location
328 of the CDF in the Central North Sea as mapped using deep regional seismic data (Abramovitz
329 and Thybo, 1999; Abramovitz and Thybo, 2000), overall extending the mapped extent of this
330 structure over 100 km into the Central North Sea (Figure 9). A number of thin intra-shear
331 zone mylonites are observed above the basal décollement (Figure 10). Based on their low dip
332 (0-10°) and overall flat-ramp geometry, we infer that these structures initially formed as
333 mylonitic Caledonian thrusts (cf. Reeve et al. (2013)).

334 A series of intrabasement packages (IP2-4), dipping at c. 30°, cross-cut the shallowly dipping
335 basal décollement of the Caledonian thrust belt (Figure 5, 6, 9). IP2 correlates along-strike to

336 the Devonian-aged extensional Karmøy Shear Zone (KSZ) observed onshore. The KSZ forms
337 a southwards splay from the Hardangerfjord Shear Zone to the north (Fossen, 2010). IP3 is
338 confidently correlated c. 30 km along-strike to the onshore Stavanger Shear Zone (SSZ).
339 These interpretations are further constrained locally by interpretations of the deep regional
340 ILP seismic data (Fossen et al., 2014). IP4 however, does not correlate to any structures
341 mapped onshore or on deep seismic reflection data; we thus propose that this represents a
342 previously undefined structure that we hereby term the Flekkefjord Shear Zone (FSZ; Figure
343 9). We infer that the FSZ splays southwards from the footwall of the KSZ, showing a similar
344 relationship to that observed between the KSZ and the Hardangerfjord Shear Zone further
345 north (Figure 9, 11).

346 We have constrained the 3D geometry of a series of intrabasement structures associated with
347 the Caledonian thrust belt and Devonian extensional shear zones (Figure 9). Caledonian
348 allocthons and the associated basal décollement are observed within the hanging walls of
349 later (i.e. cross-cutting) Devonian extensional shear zones. A number of these shear zones
350 splay southwards, potentially merging at depth and initially originating from the HSZ to the
351 north (Figure 9).

352 **5. Reactivation of intrabasement structures**

353 Using our detailed 3D framework of intrabasement structure, combined with seismic-
354 stratigraphic analysis of the sedimentary cover, we now investigate the reactivation of these
355 structures during post-Devonian tectonic events and examine how this has affected the
356 geometry and evolution of the superposed rift.

357 **5.1. Reactivation of Caledonian thrust structures**

358 We map a series of thin intra-shear zone mylonites, previously interpreted as Caledonian
359 thrusts (Figure 6), above the basal décollement and beneath a series of Lower Permian
360 depocentres (Figure 6, 10). These structures are only mapped locally on the Stavanger
361 Platform (Figure 9); further north, these thin structures are very difficult to identify and map
362 across rather sparse, relatively widely spaced 2D seismic profiles (Figure 2).

363 Two seismic facies, defining an upper and lower set of depocentres, are observed within the
364 hanging wall of some of the interpreted Caledonian thrusts (Figure 10), indicating some
365 extensional reactivation along these structures. The upper depocentres are typically 2-4 km
366 in diameter and around 100 ms thick (c. 130 m). They display higher amplitudes than the
367 lower depocentres and surrounding seismic facies (Figure 10). The upper depocentres are
368 truncated by the overlying Base Cretaceous Unconformity (BCU) and internal reflections
369 onlap onto the underlying strata (Figure 10). The lower depocentres are truncated and
370 separated from the upper depocentres by an unconformity of unknown age. The lower
371 depocentres are typically of lower amplitude than those above, forming a unit c. 200 ms (c.
372 300 m) thick, although the boundary with the underlying basement is often unclear (Figure
373 10). Wedge-shaped stratal geometries are observed locally, thickening towards the
374 Caledonian thrusts (Figure 10).

375 We interpret that the lower depocentres formed during an early phase of extensional
376 reactivation along the Caledonian thrusts. The age of the strata flanking these structures and
377 therefore the timing of the extensional reactivation of the Caledonian thrusts is unknown due
378 to a lack of well penetration and erosion associated with the BCU (Figure 10). However,
379 these structures may have undergone extensional reactivation during the initial stages of
380 Devonian orogenic collapse (Mode I), when extension was accommodated through
381 backsliding of the orogenic wedge and reactivation of Caledonian structures (Fossen, 1992).
382 During this extension, the mylonitic shear zones may have formed weaknesses within the

383 nappe sequence, acting to localise strain and preferentially reactivating; leading to the
384 development of the lower depocentres. We speculate that the high-amplitude upper
385 depocentres may have formed during a later period of brittle extension, with the bounding
386 structures, the extensionally reactivated Caledonian thrusts, having been weakened during the
387 first phase of reactivation.

388 A later phase of reverse reactivation is observed along some of the structures, as indicated by
389 the presence of a raised depocentre bounded by two Caledonian thrusts and an accompanying
390 inversion monocline (Figure 10). The BCU is gently folded across this monocline, indicating
391 the structure is post-Cretaceous in age. We suggest that the causal compressional event may
392 have occurred during the Upper Cretaceous, potentially related to the Alpine inversion
393 (Figure 5) (Biddle and Rudolph, 1988; Cartwright, 1989; Jackson et al., 2013).

394 As described above, we observe extensional and compressional reactivation of individual
395 Caledonian thrusts. However, the depocentres resulting from this reactivation are relatively
396 minor compared to the main rift-related faults and do not affect the large-scale rift
397 morphology. It appears that Mode I Devonian extension had a negligible impact on the
398 overall evolution of the rift, especially in comparison to the formation of the large-scale
399 Devonian Shear Zones during subsequent Mode II extension, as described below.

400 **5.2. Reactivation of Devonian shear zones**

401 In addition to that described in the previous section, we also observe multiple phases of
402 reactivation of Devonian extensional shear zones. Along the KSZ we observe Triassic strata
403 that thicken across a series of faults rooted into internal planes within the shear zone (Figure
404 7, 11). In addition, across-fault thickening and wedge-shaped stratal geometries are observed
405 in Triassic strata in the hanging wall of the Flekkefjord Shear Zone (FSZ) (Figure 11). This
406 indicates that both structures underwent extensional reactivation during the Triassic.

407 Furthermore, a series of salt walls are located above the intrabasement structures in the south
408 (Figure 8); Triassic extensional reactivation of the underlying intrabasement structures may
409 have led to salt mobilisation and the formation of overlying salt walls (Koyi and Petersen,
410 1992). Jurassic and Lower Cretaceous strata also thicken across the FSZ, though they are
411 largely isopachous across the KSZ. Slight thickening of Lower Cretaceous strata is observed
412 across the KSZ in the Stavanger Ramp area (Figure 11), although the majority of extension in
413 this area was accommodated by the FSZ rather than the KSZ. The KSZ accommodates large
414 amounts of extension in the north beneath the Åsta Graben where the FSZ is not present
415 (Figure 12), whereas to the south extension is initially distributed between the KSZ and FSZ
416 (Figure 7, 11), and then solely accommodated by the FSZ (Figure 8). Bøe et al. (2011)
417 propose further evidence for the Jurassic extensional reactivation of the KSZ, with the
418 Karmsundet Basin, offshore Karmøy island, formed through extensional reactivation of the
419 KSZ.

420 A NE-facing, NW-SE-striking monocline is observed above the FSZ (Figure 11). Upper
421 Cretaceous strata onlap the forelimb of the monocline, indicating it formed during the Late
422 Cretaceous. Similarly oriented structures are observed in this part of the North Sea (Biddle
423 and Rudolph, 1988; Cartwright, 1989; Thybo, 2000; Jackson et al., 2013). For example,
424 Jackson et al. (2013) observe inversion-related anticlines directly along-strike to the south,
425 above the Stavanger Fault System (Figure 7). These folds initiated during the latest Turonian-
426 to-earliest Coniacian and the Santonian, and were caused by NE-directed compression
427 resulting from the Alpine Orogeny (Jackson et al., 2013). The observed monocline above the
428 FSZ forms a continuation of this structure to the NW, with reactivation occurring along a
429 fault related to the FSZ as opposed to the Stavanger Fault System.

430 **6. Relationships between intrabasement structures and rift-related faults**

431 We note a strong plan-view correlation between the location and orientation of the
432 intrabasement structures at top basement level and the location and orientation of the later
433 rift-related faults (Figure 9). For example, the Stavanger Fault System and the Lista fault
434 blocks follow the same trend as the underlying SSZ and CDF respectively (Figure 9);
435 likewise, the Åsta Fault shares the orientation and polarity of the underlying KSZ (Figure 9).
436 Similar correlations between basement structures and rift-related faults have previously been
437 noted in plan-view (Younes and McClay, 2002; Bellahsen et al., 2013; Fossen et al., 2016),
438 with faults inheriting pre-existing structures that are oriented oblique to the regional stress
439 field. Examining these relationships in cross section, we observe a range of interaction styles
440 between the intrabasement structures and the later rift-related faults: i) ‘merging faults’ that
441 join along the margin of the shear zone at depth (e.g. between the KSZ and the Åsta fault;
442 Figure 12); ii) ‘exploitative faults’ that root into internal planes at the underlying shear zone
443 subcrops (e.g. above the FSZ; see Figure 11; and above the SSZ; see Figure 5); and iii)
444 ‘cross-cutting faults’ that form independently from and are unaffected by any underlying
445 basement structure (e.g. where the Sele High Fault System cross-cuts the KSZ; Figure 13).
446 We here provide detailed descriptions of these three interaction styles between the
447 intrabasement structure and rift-related faults.

448 **6.1 Faults merging along the margin of shear zones at depth**

449 Some rift-related faults are located within the hangingwall of intrabasement structures,
450 following their orientation and dip direction in map view (Figure 9), and merging along the
451 margins of these structures at depth (Figure 12). The upper part of the shear zone subcrops
452 within the footwall of the younger rift-related fault. For example, the Åsta fault is situated
453 above the KSZ, soling down into the margin of the structure at c. 3 s TWT (c. 4 km). Triassic
454 strata are largely restricted to the hanging wall of the Åsta fault, indicating that this structure
455 may have been active during the Permo-Triassic rift event. Jurassic and Lower Cretaceous

456 strata also thicken across the Åsta fault, indicating that the fault was also active during the
457 Jurassic and Early Cretaceous, and that the KSZ was reactivated during Late Jurassic-Early
458 Cretaceous rifting (Figure 12). In addition, a wedge-shaped package of reflections occurs
459 within the Åsta Graben, with this package truncated along the base Triassic along at its top
460 (Figure 12). We infer this package records a pre-Triassic, potentially Carboniferous-Permian
461 period of extension (Sørensen et al., 1992; Ziegler, 1992).

462 **6.2 Faults exploiting internal planes within shear zones**

463 Some rift-related faults link downward into discrete planes within the intrabasement shear
464 zones, as observed in association with IP4 (Figure 7), the KSZ (Figure 11) and the SSZ
465 (Figure 5). In these instances we infer that reactivation occurs internally within the shear
466 zone, potentially exploiting weak internal mylonite zones, forming a fault that then
467 propagates upwards into the cover. Furthermore, in the locations where the shear zones are
468 truncated at top basement a number of minor depocentres and extensional top-basement
469 offsets are observed, suggesting extension along internal planes within the shear zone (Figure
470 5, 12).

471 As previously described, the Stavanger Basin is located within the Stavanger Platform
472 (Figure 1), directly above the Stavanger Shear Zone (Figure 5, 9). Due to a lack of well
473 control across the Stavanger Platform we are unable to directly determine the age of the
474 contained sediments, although a Permo-Triassic rift age seems likely, which is consistent
475 with the Stavanger Fault System along strike to the south (Figure 9). The shear zones offset
476 the basal décollement of the Caledonian thrust belt. A series of faults bound the overlying
477 depocentre and exploit internal planes within the underlying shear zone. In addition, two
478 large lozenge-shaped reflection packages are observed within the shear zone, bound by faults
479 (Figure 5).

480 To the south, a similar exploitative interaction is proposed for the relationship between the
481 Stavanger Fault System and the SSZ (Figure 9), although this is not as well imaged in our
482 seismic data (Figure 7). The Stavanger Fault System has previously been interpreted to
483 represent a reactivated Caledonian thrust (Sørensen et al., 1992); however, based on our
484 interpretation and mapping of the structure (Figure 9), along with similar relationships
485 observed to the north (Figure 5), we take to be the basal décollement of the Caledonian thrust
486 belt for the southern fault segment (Figure 9), and the SSZ for the northern segment (Figure
487 6). The presence of Permian Zechstein salt in the area often complicates the stratal
488 geometries; however, where salt is largely absent, we observe that Triassic strata thicken
489 towards the faults, indicating that they were active at this time (Figure 7). In addition,
490 Jackson et al. (2013), observe the formation of an inversion-related anticline above the fault
491 (Figure 7), indicating that the fault, and therefore potentially the SSZ, underwent reverse
492 reactivation during Late Cretaceous compression.

493 **6.3 Faults cross-cutting intrabasement structure**

494 Although many intrabasement structures and rift-related cover structures are often
495 geometrically and kinematically linked, as described in the previous two sections, we also
496 observe instances where the two are seemingly unrelated, with the latter cross-cutting the
497 former. The Sele High Fault System is situated between the subcrops of the KSZ to the east
498 and the HSZ to the northwest. This fault system strikes N-S, and dips c. 60°E. At c. 5 s TWT
499 the fault cross-cuts the underlying KSZ, offsetting the structure by c. 2 s TWT (c. 3.5 km)
500 (Figure 13). A further fault is observed within the footwall of the Sele High Fault System,
501 offsetting an earlier formed, potentially Carboniferous basin (Sørensen et al., 1992), and
502 appearing to terminate at the KSZ (Figure 13).

503 **7. Discussion**

504 **7.1 3D Geometry and inter-relationships between intrabasement structures**

505 The Caledonian thrust belt was cross-cut by extensional Devonian shear zones during
506 orogenic collapse of the Caledonides (Fossen, 2010). We observe similar relationships within
507 our data, with the basal décollement of the Caledonian thrust belt being extensionally offset
508 across the SSZ and KSZ, although it is not imaged in the downthrown hanging wall of the
509 latter (Figure 5). Distributed ductile deformation across the Stavanger Shear Zone during its
510 formation resulted in the monoclinal folding of the basal décollement and overlying
511 Caledonian nappes (*sensu* Fossen and Hurich, 2005). Subsequently, during a later, most
512 likely Permo-Triassic rift phase, the SSZ was reactivated in a brittle manner, forming the
513 Stavanger Basin (Figure 5). The Stavanger Basin is bound by faults that exploit internal
514 planes within the shear zone. Contrary to the distributed strain associated with folding of the
515 basal décollement during the Devonian, the brittle faults exploit discrete internal planes
516 within the shear zone; this results in shearing of the basal décollement between these faults,
517 and the development of lozenge-shaped reflection packages (Figure 5) that indicate
518 extensional, sinistral shear (Ponce et al., 2013). Similar relationships are observed onshore;
519 Fossen and Hurich (2005) observe that formation of the Devonian-aged HSZ folded the
520 overlying Caledonian thrust belt. This was later exploited by the overlying brittle Lærdel-
521 Gjende fault system.

522 The newly defined FSZ forms a southward splay from the KSZ (Figure 9), mirroring the
523 relationship between the latter and the HSZ further to the north. In addition the FSZ merges
524 with the KSZ at depth (Figure 11). Fossen and Hurich (2005) propose that the HSZ represents
525 the boundary between thick-skinned to the north and thin-skinned tectonics towards the south
526 and is associated with a major Moho offset (Fossen et al., 2014). Based on our observations
527 we may speculate that the southwards splaying KSZ and FSZ join the HSZ at mid-crustal
528 depths representing a more thin-skinned component of Devonian orogenic collapse.

529 **7.2 Selective reactivation of intrabasement structure**

530 Using the 3D framework of intrabasement structure along with the seismic stratigraphic
531 architecture of the overlying rift, we are able to examine in detail the interactions between the
532 intrabasement structures and later rift-related faults throughout multiple tectonic events. Our
533 data suggest that thinner (c. 100 m) structures (i.e. Caledonian thrusts) are less likely to
534 interact with later rift-related faults than thicker (1-2 km) structures. Although we do observe
535 minor reactivation of Caledonian thrusts (Figure 10), we suggest this is linked to Mode I
536 Devonian, rather than subsequent Permo-Triassic or Jurassic-Cretaceous extension (Fossen
537 and Rykkelid, 1992), and does not affect the overall geometry and evolution of the
538 superposed rift. Reeve et al. (2013) identify similar reflection packets to the north in the
539 northern North Sea, also interpreting them as Caledonian thrusts, and find that rift-related
540 faults cross-cut and are unaffected by their presence. Similarly, Kirkpatrick et al. (2013)
541 suggest a degree of scale-dependency on the reactivation of intrabasement structures, with
542 large-scale structures preferentially reactivated and smaller structures cross-cut. We argue
543 that thicker structures are preferentially reactivated because they are more likely to contain a
544 layer weak or several weak layers, in this instance represented by intra-shear zone mylonites,
545 that may be reactivated during later rift events (White et al., 1986; Salomon et al., 2015).

546 Although the mapped intrabasement structures are all relatively low-angle ($<30^\circ$), we also
547 note, notwithstanding Devonian mode I extension, a lack of reactivation of the relatively
548 shallow-dipping (c. 10°), albeit relatively thick (c. 1-2 km) intrabasement structures, such as
549 the basal décollement. Conversely, we observe multiple phases of reactivation along the
550 steeper (c. 30°), relatively thick (c. 1-2 km) Devonian shear zones (Figure 5, 12). Therefore,
551 in addition to thicker structures being preferentially reactivated, we suggest that steeper
552 structures are also preferentially reactivated over shallow ones, in accordance with
553 theoretical considerations (Sibson, 1985). The orientation of intrabasement structures relative

554 to the regional stress field may also play a role in their selective reactivation (Ring, 1994;
555 Morley et al., 2004; Henza et al., 2011), although we are unable to assess this factor as the
556 studied intrabasement structures all roughly trend N-S and dip westward.

557 Finally, we find that previously reactivated structures are consequently weakened and
558 therefore more likely to reactivate during a later tectonic event. For example, IP4 initially
559 formed as an extensional structure during the Devonian, underwent extensional reactivation
560 during Permo-Triassic rifting, was further extensionally reactivated during the Late Jurassic-
561 Early Cretaceous rift phase, and finally underwent reverse reactivation in response to Late
562 Cretaceous compression (Figure 6, 11).

563 **7.3 Fault-intrabasement structure interactions**

564 We observe three main styles of interaction between rift-related faults and underlying
565 Devonian shear zones (e.g. ‘merging’, ‘exploitative’, and ‘cross-cutting’ faults; see Figure
566 14).

567 Exploitative faults are observed along IP4, the KSZ and the SSZ (Figure 5, 8, 9), rooting into
568 internal reflection planes interpreted as layered sequences of highly strained mylonites and
569 relatively undeformed rock. The mylonitic foliation, along with the overall layering, mean the
570 shear zone is strongly mechanically anisotropic, with the mylonite zones being weaker than
571 the surrounding relatively undeformed rocks (White et al., 1980; Chattopadhyay and Chakra,
572 2013). This strong heterogeneity may be preferentially exploited during later brittle
573 reactivation of the shear zones (Gontijo-Pascutti et al., 2010; Salomon et al., 2015; Scheiber
574 et al., 2015). In addition, varying thicknesses of mylonite zones and the degree of strain
575 experienced may have different strengths, providing multiple potential sites for later faults to
576 exploit during brittle reactivation of the shear zones.

577 The Åsta fault is an example of a merging fault interaction, joining along the margin of the
578 KSZ at depth (Figure 5, 12). What is less clear is where the rift-related fault initiates and how
579 it subsequently propagates, does it initiate at and grow upwards from the shear zone; or
580 nucleate within the hanging wall of the shear zone, before propagating downwards and
581 joining the structure at depth? In the former situation, extension may be accommodated by
582 ductile reactivation of the shear zone at depth, with the formation of a steeper fault becoming
583 preferential at shallower levels (Huyghe and Mugnier, 1992); whilst theoretically possible we
584 note that, at least within the study area, the KSZ does not reach the depths of the ductile
585 regime. In the latter situation, the shear zone acts as an intrabasement heterogeneity, acting to
586 perturb the regional stress field and localise strain, causing fault nucleation within its hanging
587 wall, with these faults inheriting the orientation and dip direction of the underlying structure.
588 Subsequent growth would then cause the faults to physically link with the underlying
589 structure. Furthermore, previous studies have shown that the dip of later rift-related faults
590 may be influenced by the dip of underlying shear zones (Ring, 1994; Salomon et al., 2015),
591 with initial fractures coalescing to produce a steeper through-going fault. Due to the reasons
592 outlined above, we prefer the latter scenario, where faults initiate above and ultimately link
593 downward with the intrabasement structures.

594 The Devonian shear zones often show rugose top basement subcrops, with minor extensional
595 exploitative faults present (Figure 9). The weak, low-angle shear zone may initially
596 accommodate small amounts of extension, forming exploitative faults (Figure 5, 13). Upon
597 further extension, the low-angle shear zone may become locked, resulting in the formation of
598 a steeper fault within the hanging wall, inheriting the geometric properties of the underlying
599 shear zone, which eventually displays a 'merging' relationship (Figure 9).

600 Cross-cutting faults, such as the Sele High Fault System (Figure 13), form in areas where
601 large intrabasement structures are lacking. Therefore they initiate in a manner similar to faults

602 forming within homogeneous material (Cowie et al., 2000; Gawthorpe and Leeder, 2000).
603 Such faults form in response to the regional stress field, perpendicular to the extension
604 direction and at typical dips of c. 60°, as opposed to in response to local perturbations
605 surrounding intrabasement structures (Figure 15). As they propagate laterally and vertically
606 the faults are at a high angle to and therefore cross-cut underlying, low-angle intrabasement
607 structures.

608 **7.4 Effects of intrabasement structure on rift geometry and evolution**

609 Rifts forming within relatively pristine (i.e. homogenous) crust are typically characterised by
610 regularly spaced, sub-parallel faults that strike perpendicular to the regional extension
611 direction (Gupta et al., 1998; Cowie et al., 2000; Gawthorpe and Leeder, 2000). However, the
612 geometry and evolution of rift basins in areas of more heterogeneous (i.e. ‘non-pristine’)
613 crust, such as those containing pre-existing, discrete intrabasement structures, differ from and
614 thus cannot be adequately described using established models of rift evolution. For example,
615 we show that large-scale Devonian shear zones act as heterogeneities within this otherwise
616 ‘pristine’ crust and, being prone to reactivation, act to locally modify the regional stress field
617 (Figure 15). These structures form a ‘template’ for fault development and thus the subsequent
618 basin structure associated with later extensional and contractional tectonic events. In addition,
619 the spacing between the reactivated intrabasement structures can also control the degree of
620 faulting that occurs. Closely spaced shear zones are able to host a wider zone of exploitative
621 faulting, with each fault rooted in an individual intra-shear zone mylonite zone. Strain is
622 therefore distributed over a wider area, leading to an overall more gently dipping rift margin
623 (Figure 11). Such a scenario is observed across the Stavanger Ramp (Figure 9), where strain
624 is distributed across a series of relatively low displacement exploitative faults atop the closely
625 spaced KSZ and FSZ (Figure 11). Due to their close-spacing within the overall shear zones,
626 not all of the intra-shear zone mylonites host an exploitative fault. This observation is in

627 agreement with Sassi et al. (1993), who observe that only selected structures are reactivated
628 when closely spaced.

629 Where large intrabasement structures are absent, rift-related faults form in response to the
630 regional stress field and cross-cut smaller intrabasement structures (Figure 14). A lack of
631 large, discrete intrabasement structures may help to explain the lack of fault-intrabasement
632 structures relationships observed in areas where the intrabasement structure is cross-cut
633 (Kirkpatrick et al., 2013; Reeve et al., 2013). Alternatively, such structures may be present in
634 other rifts, but are not imaged in seismic reflection data or resolved in potential field data.

635 **8. Conclusions**

636 Using closely spaced 2D and 3D seismic data we have resolved the 3D geometry of a series
637 of spectacularly imaged structures within crystalline basement over a 10,000 km² area
638 offshore southern Norway. These structures are correlated onshore, and are analysed in
639 context to the evolution and geometry of the overlying rift. Throughout this study, we have
640 shown that:

641 1. The characteristic reflection geometries of the intrabasement structures cannot be
642 generated by a single interface within crystalline basement. 1D waveform modelling suggests
643 that this forms through constructive interference between layers roughly 100 m thick
644 separated by 50-100 m. These layers may represent anastomosing mylonite zones separated
645 by relatively undeformed material, as observed in shear zones onshore.

646 2. Through along-strike correlations to established onshore structures, the observed
647 intrabasement structures represent the offshore continuations of the Caledonian thrust belt
648 and a series of Devonian extensional shear zones. The locations and 3D geometry of these
649 structures are constrained for over 100 km offshore beneath the North Sea rift. A further

650 shear zone, the Flekkefjord Shear Zone is newly defined and mapped offshore. The Devonian
651 shear zones offset the Caledonian thrust belt and in some cases are linked in 3D.

652 3. Selective reactivation of intrabasement structures occurs during later tectonic events,
653 exerting a strong influence over the evolution and geometry of the overlying rift. Thicker,
654 steeper structures, such as the Devonian shear zones, are preferentially reactivated at the
655 expense of thinner, more gently-dipping structures. Previously reactivated, and therefore
656 weaker, structures are then preferentially reactivated during later tectonic events.

657 4. We observe a number of interactions between the reactivated Devonian shear zones and
658 the later rift-related faults: i) Faults that form within the hanging wall of intrabasement shear
659 zones due to local stress perturbations and merge with the structures at depth; ii) faults that
660 exploit internal weaknesses, i.e. mechanical anisotropies exhibited by mylonites, within the
661 shear zones; and iii) faults that form independently away from intrabasement structure in
662 response to the regional stress field, and cross-cut underlying structure. Close proximity
663 between intrabasement structures allows strain to be distributed over a wider area, resulting in
664 multiple, low-displacement faults, and an overall gentler rift margin.

665 5. The presence of large-scale intrabasement structures acts to locally modify the regional
666 stress field, and exhibits a first-order control on the location of later rift-related faults, with
667 basin-bounding faults inheriting this pre-existing framework. Rift-related faults form in
668 response to the regional stress field in areas where this pre-existing framework is not present.
669 Characteristics such as anomalous fault geometries and local areas of distributed faulting may
670 be used to infer the presence of an underlying complexity, such as a discrete intrabasement
671 structure, especially in areas where crystalline basement is poorly imaged.

672 The geometry and distribution of underlying basement heterogeneities dictates the location of
673 many basin margins, determining the initial rift physiography and size (Figure 14). In

674 addition, the repeated reactivation of these structures shows how they play a long-lived role
675 in the evolution of the rift system throughout multiple tectonic events.

676 **Acknowledgments**

677 The authors would like to thank PGS and TGS for allowing us to show the seismic data used
678 in this study, along with Schlumberger for providing academic licences for use of Petrel
679 software. This contribution forms part of the MultiRift Project funded by the Research
680 Council of Norway's PETROMAKS programme (Project number 215591) and Statoil to the
681 University of Bergen and partners Imperial College, University of Manchester and University
682 of Oslo.

683 **References**

- 684 Abramovitz, T., Thybo, H., 1999. Pre-Zechstein structures around the MONA LISA deep seismic lines
685 in the southern Horn Graben area. *Bulletin of the Geological Society of Denmark* 10, 99-116.
- 686 Abramovitz, T., Thybo, H., 2000. Seismic images of Caledonian, lithosphere scale collision structures
687 in the southeastern North Sea along Mona Lisa Profile 2. *Tectonophysics* 317, 27-54.
- 688 Autin, J., Bellahsen, N., Leroy, S., Husson, L., Beslier, M.-O., d'Acremont, E., 2013. The role of
689 structural inheritance in oblique rifting: Insights from analogue models and application to the Gulf of
690 Aden. *Tectonophysics* 607, 51-64.
- 691 Bartholomew, I.D., Peters, J.M., Powell, C.M., 1993. Regional structural evolution of the North Sea:
692 oblique slip and the reactivation of basement lineaments. Geological Society, London, Petroleum
693 Geology Conference series 4, 1109-1122.
- 694 Bell, R.E., Jackson, C.A.L., Whipp, P.S., Clements, B., 2014. Strain migration during multiphase
695 extension: observations from the northern North Sea. *Tectonics*.
- 696 Bellahsen, N., Daniel, J.M., 2005. Fault reactivation control on normal fault growth: an experimental
697 study. *Journal of Structural Geology* 27, 769-780.
- 698 Bellahsen, N., Leroy, S., Autin, J., Razin, P., d'Acremont, E., Sloan, H., Pik, R., Ahmed, A., Khanbari, K.,
699 2013. Pre-existing oblique transfer zones and transfer/transform relationships in continental
700 margins: New insights from the southeastern Gulf of Aden, Socotra Island, Yemen. *Tectonophysics*
701 607, 32-50.
- 702 Biddle, K.T., Rudolph, K.W., 1988. Early Tertiary structural inversion in the Stord Basin, Norwegian
703 North Sea. *Journal of the Geological Society* 145, 603-611.
- 704 Bingen, B., Nordgulen, Ø., Viola, G., 2008. A four-phase model for the Sveconorwegian orogeny, SW
705 Scandinavia. *Norwegian journal of Geology* 88, 43-72.
- 706 Bird, P.C., Cartwright, J.A., Davies, T.L., 2014. Basement reactivation in the development of rift
707 basins: an example of reactivated Caledonide structures in the West Orkney Basin. *Journal of the*
708 *Geological Society* 172, 77-85.
- 709 Bladon, A.J., Clarke, S.M., Burley, S.D., 2015. Complex rift geometries resulting from inheritance of
710 pre-existing structures: Insights and regional implications from the Barmer Basin rift. *Journal of*
711 *Structural Geology* 71, 136-154.

- 712 Bøe, R., Fossen, H., Smelror, M., 2011. Mesozoic sediments and structures onshore Norway and in
713 the coastal zone. *Norges geologiske undersøkelse Bulletin* 450.
- 714 Boundy, T.M., Fountain, D.M., Austrheim, H., 1992. Structural development and petrofabrics of
715 eclogite facies shear zones, Bergen Arcs, western Norway: implications for deep crustal
716 deformational processes. *Journal of Metamorphic Geology* 10, 127-146.
- 717 Brun, J.-P., Tron, V., 1993. Development of the North Viking Graben: inferences from laboratory
718 modelling. *Sedimentary Geology* 86, 31-51.
- 719 Carreras, J., 2001. Zooming on Northern Cap de Creus shear zones. *Journal of Structural Geology* 23,
720 1457-1486.
- 721 Carreras, J., Czeck, D.M., Druguet, E., Hudleston, P.J., 2010. Structure and development of an
722 anastomosing network of ductile shear zones. *Journal of Structural Geology* 32, 656-666.
- 723 Cartwright, J.A., 1989. The kinematics of inversion in the Danish Central Graben. Geological Society,
724 London, Special Publications 44, 153-175.
- 725 Chadwick, R.A., Kenolty, N., Whittaker, A., 1983. Crustal structure beneath southern England from
726 deep seismic reflection profiles. *Journal of the Geological Society* 140, 893-911.
- 727 Chattopadhyay, A., Chakra, M., 2013. Influence of pre-existing pervasive fabrics on fault patterns
728 during orthogonal and oblique rifting: An experimental approach. *Marine and Petroleum Geology*
729 39, 74-91.
- 730 Choukroune, P., 1989. The ECORS Pyrenean deep seismic profile reflection data and the overall
731 structure of an orogenic belt. *Tectonics* 8, 23-39.
- 732 Choukroune, P., Gapais, D., 1983. Strain Patterns in Rocks Strain pattern in the Aar Granite (Central
733 Alps): Orthogneiss developed by bulk inhomogeneous flattening. *Journal of Structural Geology* 5,
734 411-418.
- 735 Clemson, J., Cartwright, J., Booth, J., 1997. Structural segmentation and the influence of basement
736 structure on the Namibian passive margin. *Journal of the Geological Society* 154, 477-482.
- 737 Corfu, F., Andersen, T.B., Gasser, D., 2014. The Scandinavian Caledonides: main features, conceptual
738 advances and critical questions. Geological Society, London, Special Publications.
- 739 Coward, M.P., Dewey, J.F., Hempton, M., Holroyd, J., 2003. Tectonic evolution, in: Evans, D.,
740 Graham, C., Armour, A., Bathurst, P. (Eds.), *The Millenium Atlas: petroleum geology of the central
741 and northern North Sea*, Geological Society of London.
- 742 Cowie, P.A., Gupta, S., Dawers, N.H., 2000. Implications of fault array evolution for synrift depocentre
743 development: insights from a numerical fault growth model. *Basin Research* 12, 241-261.
- 744 Daly, M.C., Chorowicz, J., Fairhead, J.D., 1989. Rift basin evolution in Africa: the influence of
745 reactivated steep basement shear zones. *Geol Soc London, Special Publication* 44, 309-334.
- 746 Dewey, J.F., 1988. Extensional collapse of orogens. *Tectonics* 7, 1123-1139.
- 747 Doré, A.G., Lundin, E.R., Fichler, C., Olesen, O., 1997. Patterns of basement structure and
748 reactivation along the NE Atlantic margin. *Journal of the Geological Society* 154, 85-92.
- 749 Druguet, E., Passchier, C.W., Carreras, J., Victor, P., den Brok, S., 1997. Analysis of a complex high-
750 strain zone at Cap de Creus, Spain. *Tectonophysics* 280, 31-45.
- 751 Duffy, O.B., Bell, R.E., Jackson, C.A.L., Gawthorpe, R.L., Whipp, P.S., 2015. Fault growth and
752 interactions in a multiphase rift fault network: Horda Platform, Norwegian North Sea. *Journal of
753 Structural Geology* 80, 99-119.
- 754 Faccenna, C., Nalpas, T., Brun, J.-P., Davy, P., Bosi, V., 1995. The influence of pre-existing thrust faults
755 on normal fault geometry in nature and in experiments. *Journal of Structural Geology* 17, 1139-1149.
- 756 Færseth, R.B., 1996. Interaction of Permo-Triassic and Jurassic extensional fault-blocks during the
757 development of the northern North Sea. *Journal of the Geological Society* 153, 931-944.
- 758 Færseth, R.B., Knudsen, B.E., Liljedahl, T., Midbøe, P.S., Söderstrøm, B., 1997. Oblique rifting and
759 sequential faulting in the Jurassic development of the northern North Sea. *Journal of Structural
760 Geology* 19, 1285-1302.
- 761 Fossen, H., 1992. The role of extensional tectonics in the Caledonides of south Norway. *Journal of
762 Structural Geology* 14, 1033-1046.

- 763 Fossen, H., 2010. Extensional tectonics in the North Atlantic Caledonides: a regional view. Geological
764 Society, London, Special Publications 335, 767-793.
- 765 Fossen, H., Dunlap, J.W., 1998. Timing and kinematics of Caledonian thrusting and extensional
766 collapse, southern Norway: evidence from $^{40}\text{Ar}/^{39}\text{Ar}$ thermochronology. *Journal of Structural*
767 *Geology* 20, 765-781.
- 768 Fossen, H., Gabrielsen, R.H., Faleide, J.I., Hurich, C.A., 2014. Crustal stretching in the Scandinavian
769 Caledonides as revealed by deep seismic data. *Geology* 42, 791-794.
- 770 Fossen, H., Hurich, C.A., 2005. The Hardangerfjord Shear Zone in SW Norway and the North Sea: a
771 large-scale low-angle shear zone in the Caledonian crust. *Journal of the Geological Society* 162, 675-
772 687.
- 773 Fossen, H., Khani, H.F., Faleide, J.I., Ksienzyk, A.K., Dunlap, W.J., 2016. Post-Caledonian extension in
774 the West Norway–northern North Sea region: the role of structural inheritance. Geological Society,
775 London, Special Publications 439.
- 776 Fossen, H., Rykkelid, E., 1992. Postcollisional extension of the Caledonide orogen in Scandinavia:
777 Structural expressions and tectonic significance. *Geology* 20, 737.
- 778 Fountain, D.M., Hurich, C.A., Smithson, S.B., 1984. Seismic reflectivity of mylonite zones in the crust.
779 *Geology* 12, 195.
- 780 Fraser, A.J., Gawthorpe, R.L., 1990. Tectono-stratigraphic development and hydrocarbon habitat of
781 the Carboniferous in northern England. Geological Society, London, Special Publications 55, 49-86.
- 782 Gabrielsen, R.H., Braathen, A., Dehls, J., Roberts, D., 2002. Tectonic Lineaments of Norway.
783 *Norwegian journal of Geology* 82, 153-174.
- 784 Gawthorpe, R.L., Leeder, M.R., 2000. Tectono-sedimentary evolution of active extensional basins.
785 *Basin Research* 12, 195-218.
- 786 Gontijo-Pascutti, A., Bezerra, F.H.R., Terra, E.L., Almeida, J.C.H., 2010. Brittle reactivation of mylonitic
787 fabric and the origin of the Cenozoic Rio Santana Graben, southeastern Brazil. *Journal of South*
788 *American Earth Sciences* 29, 522-536.
- 789 Goscombe, B., Hand, M., Gray, D., 2003. Structure of the Kaoko Belt, Namibia: progressive evolution
790 of a classic transpressional orogen. *Journal of Structural Geology* 25, 1049-1081.
- 791 Goscombe, B.D., Gray, D.R., 2008. Structure and strain variation at mid-crustal levels in a
792 transpressional orogen: A review of Kaoko Belt structure and the character of West Gondwana
793 amalgamation and dispersal. *Gondwana Research* 13, 45-85.
- 794 Gupta, S., Cowie, P.A., Dawers, N.H., Underhill, J.R., 1998. A mechanism to explain rift-basin
795 subsidence and stratigraphic patterns through fault-array evolution. *Geology* 26, 595-598.
- 796 Hedin, P., Juhlin, C., Gee, D.G., 2012. Seismic imaging of the Scandinavian Caledonides to define ICDP
797 drilling sites. *Tectonophysics* 554–557, 30-41.
- 798 Henza, A.A., Withjack, M.O., Schlische, R.W., 2011. How do the properties of a pre-existing normal-
799 fault population influence fault development during a subsequent phase of extension? *Journal of*
800 *Structural Geology* 33, 1312-1324.
- 801 Hurich, C.A., Smithson, S.B., Fountain, D.M., Humphreys, M.C., 1985. Seismic evidence of mylonite
802 reflectivity and deep structure in the Kettle dome metamorphic core complex, Washington. *Geology*
803 13, 577-580.
- 804 Huuse, M., 2002. Cenozoic uplift and denudation of southern Norway: insights from the North Sea
805 Basin. Geological Society, London, Special Publications 196, 209-233.
- 806 Huyghe, P., Mugnier, J.-L., 1992. The influence of depth on reactivation in normal faulting. *Journal of*
807 *Structural Geology* 14, 991-998.
- 808 Jackson, C.A.L., Chua, S.T., Bell, R.E., Magee, C., 2013. Structural style and early stage growth of
809 inversion structures: 3D seismic insights from the Egersund Basin, offshore Norway. *Journal of*
810 *Structural Geology* 46, 167-185.
- 811 Jackson, C.A.L., Lewis, M.M., 2013. Physiography of the NE margin of the Permian Salt Basin: new
812 insights from 3D seismic reflection data. *Journal of the Geological Society* 170, 857-860.

- 813 Jackson, C.A.L., Lewis, M.M., 2015. Structural style and evolution of a salt-influenced rift basin
814 margin; the impact of variations in salt composition and the role of polyphase extension. *Basin*
815 *Research*, n/a-n/a.
- 816 Japsen, P., Bidstrup, T., Lidmar-Bergström, K., 2002. Neogene uplift and erosion of southern
817 Scandinavia induced by the rise of the South Swedish Dome. *Geological Society, London, Special*
818 *Publications* 196, 183-207.
- 819 Kirkpatrick, J.D., Bezerra, F.H.R., Shipton, Z.K., Do Nascimento, A.F., Pytharouli, S.I., Lunn, R.J., Soden,
820 A.M., 2013. Scale-dependent influence of pre-existing basement shear zones on rift faulting: a case
821 study from NE Brazil. *Journal of the Geological Society* 170, 237-247.
- 822 Koyi, H., Petersen, K., 1992. Influence of basement faults on the development of salt structures in the
823 Danish Basin. *Marine and Petroleum Geology* 10, 82-94.
- 824 Lorenz, H., Rosberg, J.E., Juhlin, C., Bjelm, L., Almqvist, B.S.G., Berthet, T., Conze, R., Gee, D.G.,
825 Klonowska, I., Pascal, C., Pedersen, K., Roberts, N.M.W., Tsang, C.F., 2015. COSC-1 – drilling of a
826 subduction-related allochthon in the Palaeozoic Caledonide orogen of Scandinavia. *Sci. Dril.* 19, 1-11.
- 827 Lundmark, A.M., Saether, T., Sorlie, R., 2013. Ordovician to Silurian magmatism on the Utsira High,
828 North Sea: implications for correlations between the onshore and offshore Caledonides. *Geological*
829 *Society, London, Special Publications*.
- 830 Maurin, J.-C., Guiraud, R., 1993. Basement control in the development of the Early Cretaceous West
831 and Central African Rift System. *Tectonophysics* 228, 81-95.
- 832 McClay, Norton, M.G., Coney, P., Davis, G.H., 1986. Collapse of the Caledonian orogen and the Old
833 Red Sandstone. *Nature* 323, 147-149.
- 834 McKerrow, W.S., MacNiocaill, C., Dewey, J.F., 2000. The Caledonian Orogeny redefined. *Journal of*
835 *the Geological Society, London* 157, 1149-1154.
- 836 Milnes, A.G., Wennberg, O.P., Skår, Ø., Koestler, A.G., 1997. Contraction, extension and timing in the
837 South Norwegian Caledonides: the Sognefjord transect. *Geol Soc London, Special Publication* 121,
838 123-148.
- 839 Mogensen, T.E., Korstgård, J.A., 2003. Triassic and Jurassic transtension along part of the Sorgenfrei-
840 Tornquist Zone in the Danish Kattegat. *Geological Survey of Denmark and Greenland Bulletin* 1, 439-
841 458.
- 842 Morley, C.K., 1986. The Caledonian thrust front and palinspastic restorations in the southern
843 Norwegian Caledonides. *Journal of Structural Geology* 8, 753-765.
- 844 Morley, C.K., Haranya, C., Phoosongsee, W., Pongwapee, S., Kornsawan, A., Wonganan, N., 2004.
845 Activation of rift oblique and rift parallel pre-existing fabrics during extension and their effect on
846 deformation style: examples from the rifts of Thailand. *Journal of Structural Geology* 26, 1803-1829.
- 847 Odinsen, T., Reemst, P., Beek, P.V.D., Faleide, J.I., Gabrielsen, R.H., 2000. Permo-Triassic and Jurassic
848 extension in the northern North Sea: results from tectonostratigraphic forward modelling.
849 *Geological Society, London, Special Publications* 167, 83-103.
- 850 Olesen, O., Smethurst, M.A., Torsvik, T.H., Bidstrup, T., 2004. Sveconorwegian igneous complexes
851 beneath the Norwegian–Danish Basin. *Tectonophysics* 387, 105-130.
- 852 Paton, D.A., Underhill, J.R., 2004. Role of crustal anisotropy in modifying the structural and
853 sedimentological evolution of extensional basins: the Gamtoos Basin, South Africa. *Basin Research*
854 16, 339-359.
- 855 Pedersen, R.B., Hertogen, J., 1990. Magmatic evolution of the Karmøy Ophiolite Complex, SW
856 Norway: relationships between MORB-IAT-boninitic-calc-alkaline and alkaline magmatism.
857 *Contributions to Mineralogy and Petrology* 104, 277-293.
- 858 Ponce, C., Druguet, E., Carreras, J., 2013. Development of shear zone-related lozenges in foliated
859 rocks. *Journal of Structural Geology* 50, 176-186.
- 860 Reeve, M.T., Bell, R.E., Jackson, C.A.L., 2013. Origin and significance of intra-basement seismic
861 reflections offshore western Norway. *Journal of the Geological Society*.
- 862 Rennie, S.F., Fagereng, Å., Diener, J.F.A., 2013. Strain distribution within a km-scale, mid-crustal
863 shear zone: The Kuckaus Mylonite Zone, Namibia. *Journal of Structural Geology* 56, 57-69.

- 864 Ring, U., 1994. The influence of preexisting structure on the evolution of the Cenozoic Malawi rift
 865 (East African rift system). *Tectonics* 13, 313-326.
- 866 Roffeis, C., Corfu, F., 2013. Caledonian nappes of southern Norway and their correlation with
 867 Sveconorwegian basement domains. Geological Society, London, Special Publications.
- 868 Salomon, E., Koehn, D., Passchier, C., 2015. Brittle reactivation of ductile shear zones in NW Namibia
 869 in relation to South Atlantic rifting. *Tectonics* 34, 70-85.
- 870 Sassi, W., Colletta, B., Balé, P., Paquereau, T., 1993. The origin of sedimentary basins: Inferences
 871 from quantitative modelling and basin analysis Modelling of structural complexity in sedimentary
 872 basins: The role of pre-existing faults in thrust tectonics. *Tectonophysics* 226, 97-112.
- 873 Scheiber, T., Viola, G., Bingen, B., Peters, M., Solli, A., 2015. Multiple reactivation and strain
 874 localization along a Proterozoic orogen-scale deformation zone: The Kongsberg-Telemark boundary
 875 in southern Norway revisited. *Precambrian Research* 265, 78-103.
- 876 Sibson, R.H., 1985. A note on fault reactivation. *Journal of Structural Geology* 7, 751-754.
- 877 Sørensen, S., Morizot, H., Skottheim, S., 1992. A tectonostratigraphic analysis of the southeast
 878 Northern North Sea Basin, in: Larsen, R.M., Brekke, H., Larsen, B.T., Talleraas, E. (Eds.), *Structural and*
 879 *Tectonic modelling and its application to Petroleum Geology*. Elsevier, Amsterdam, pp. 19-42.
- 880 Thybo, H., 2000. Crustal structure and tectonic evolution of the Tornquist Fan region as revealed by
 881 geophysical methods. *Bulletin of the Geological Society of Denmark* 46, 145-160.
- 882 Tong, H., Koyi, H., Huang, S., Zhao, H., 2014. The effect of multiple pre-existing weaknesses on
 883 formation and evolution of faults in extended sandbox models. *Tectonophysics* 626, 197-212.
- 884 Torvela, T., Moreau, J., Butler, R.W.H., Korja, A., Heikkinen, P., 2013. The mode of deformation in the
 885 orogenic mid-crust revealed by seismic attribute analysis. *Geochemistry, Geophysics, Geosystems*.
 886 Underhill, J.R., Partington, M.A., 1993. Jurassic thermal doming and deflation in the North Sea:
 887 implications of the sequence stratigraphic evidence. 337-345.
- 888 Vetti, V.V., Fossen, H., 2012. Origin of contrasting Devonian supradetachment basin types in the
 889 Scandinavian Caledonides. *Geology* 40, 571-574.
- 890 Wang, C.-Y., Okaya, D.A., Ruppert, C., Davis, G.A., Guo, T.-S., Zhong, Z., Wenk, H.-R., 1989. Seismic
 891 reflectivity of the Whipple Mountain shear zone in southern California. *Journal of Geophysical*
 892 *Research* 94, 2989.
- 893 Whipp, P.S., Jackson, C.A.L., Gawthorpe, R.L., Dreyer, T., Quinn, D., 2014. Normal fault array
 894 evolution above a reactivated rift fabric; a subsurface example from the northern Horda Platform,
 895 Norwegian North Sea. *Basin Research*.
- 896 White, S.H., Bretan, P.G., Rutter, E.H., 1986. Fault-Zone Reactivation: Kinematics and Mechanisms.
 897 *Philosophical Transactions of the Royal Society of London A: Mathematical, Physical and Engineering*
 898 *Sciences* 317, 81-97.
- 899 White, S.H., Burrows, S.E., Carreras, J., Shaw, N.D., Humphreys, F.J., 1980. Shear zones in rocks On
 900 mylonites in ductile shear zones. *Journal of Structural Geology* 2, 175-187.
- 901 Younes, A.I., McClay, K., 2002. Development of accommodation zones in the Gulf of Suez-Red Sea
 902 rift, Egypt. *AAPG Bulletin* 86, 1003-1026.
- 903 Ziegler, P.A., 1992. North Sea Rift System. *Tectonophysics* 208, 55-75.

904

905 **Figure Captions**

906 **Figure 1** - Figure showing the location of the study area (white box) in relation to offshore
 907 structural domains within the south eastern North Sea, as established through seismic
 908 interpretation. Structural domains are based upon the base Zechstein surface. Also shown is

909 the mapped onshore geology, taken from Fossen et al. (2014). The locations of major
910 Devonian shear zones onshore are shown in green.

911 **Figure 2** - Map showing the available datasets for use throughout this study; including 2D
912 and 3D seismic data, along with borehole data.

913 **Figure 3** - Stratigraphic framework within the study area showing the key seismic horizons
914 interpreted throughout this study, along with the major tectonic events to have affected the
915 region. Horizon colours are consistent and referred to throughout the text.

916 **Figure 4** – A) Panels showing the observed types of intrabasement reflectivity. 1) Shows the
917 observed thin intrabasement reflections packets, and 2) shows the thicker (Km-scale)
918 intrabasement packages. B) 1D waveform models of the observed reflection patterns.
919 Multiple models of layered sequences of varying thicknesses are created and then
920 subsequently compared to the observed reflection wavetrain. Individual layer thicknesses of
921 100 m, separated by 50-100 m produce the best match to the observed data.

922 **Figure 5** - Interpreted seismic section showing the large-scale structure and inter-
923 relationships between intrabasement structures. A series of steeply dipping structures can be
924 observed to cross-cut a relatively flat-lying structure. Inset – close-up of the cross-cutting
925 relationship observed in the centre of the image. See figure 1 for location.

926 **Figure 6** - Uninterpreted and interpreted seismic sections showing intrabasement structure
927 throughout the area. Larger intrabasement packages are shown in light grey with individual
928 thin intrabasement reflection packets highlighted by black dashed lines. Intrabasement
929 packages are mapped across the area, and linked along-strike to those shown in Figures 5, 7
930 and 8. A close-up of the right side of the image is shown in figure 10. Colours within the
931 sedimentary cover correspond to ages shown within the stratigraphic column (Figure 3) See
932 figure 1 for location.

933 **Figure 7** - Uninterpreted and interpreted regional seismic sections showing the geometry and
934 reactivation of intrabasement structure within the region. Intrabasement structures are
935 mapped across the area, and linked along-strike to those shown in Figures 5, 6 and 8. See
936 figure 1 for location.

937 **Figure 8** - Uninterpreted and interpreted seismic sections showing the regional intrabasement
938 structure in the south of the study area. A series of splays can be observed originating from
939 the base of IP4. See section 5 for details on the reactivation of these structures. See figure 1
940 for location.

941 **Figure 9** - Map showing the location of intrabasement structures across the study area.
942 Surface shown is the top acoustic basement time-structure map, highlighting the major
943 structural elements within the region, see figure 1 for more details. Also shown are the
944 locations of the structures as constrained by Fossen et al. (2014) (onshore and immediate
945 offshore locations), and Abramovitz and Thybo (2000) (Central North Sea). Note the
946 similarities in location between the intrabasement structures and the later rift-related faults.

947 **Figure 10** - Uninterpreted and interpreted seismic sections showing the location of the basal
948 décollement and associated Caledonian thrusts. A series of depocentres are observed in the
949 hangingwall of these structures, indicating extensional reactivation; some of which are
950 uplifted, indicative of later reverse reactivation. See figure 1 for location.

951 **Figure 11** - Uninterpreted and interpreted seismic sections highlighting multiple stages of
952 reactivation along the KSZ and FSZ beneath the Stavanger ramp area and. Seismic
953 stratigraphic relationships are used to constrain the timing of reactivation. See figure 1 for
954 location.

955 **Figure 12** - Uninterpreted and interpreted seismic sections showing the relationship between
956 the Åsta fault and the underlying KSZ, displaying a ‘merging’ type fault relationship. The

957 Åsta fault can be observed to sole onto the margin of the KSZ at depth. See figure 1 for
958 location.

959 **Figure 13** - Uninterpreted and interpreted seismic sections highlighting the interaction
960 between the Sele High Fault System and the KSZ, displaying a 'cross-cutting' relationship.
961 The SHFS can be observed to cross-cut the underlying KSZ. See figure 1 for location.

962 **Figure 14** - Schematic models showing the 3 major types of interactions between
963 intrabasement structures and rift-related faults. From left to right; Merging faults,
964 Exploitative faults and cross-cutting faults.

965 **Figure 15** - Synoptic figure showing how the presence of discrete intrabasement structures
966 may modify the geometry and evolution of overlying rift systems. Upper panel shows pre-rift
967 framework of structures within crystalline basement. Upon later extension these act to create
968 localised perturbations in the regional stress field, producing a range of interactions with the
969 rift-related faults.

970

971

972

973

974

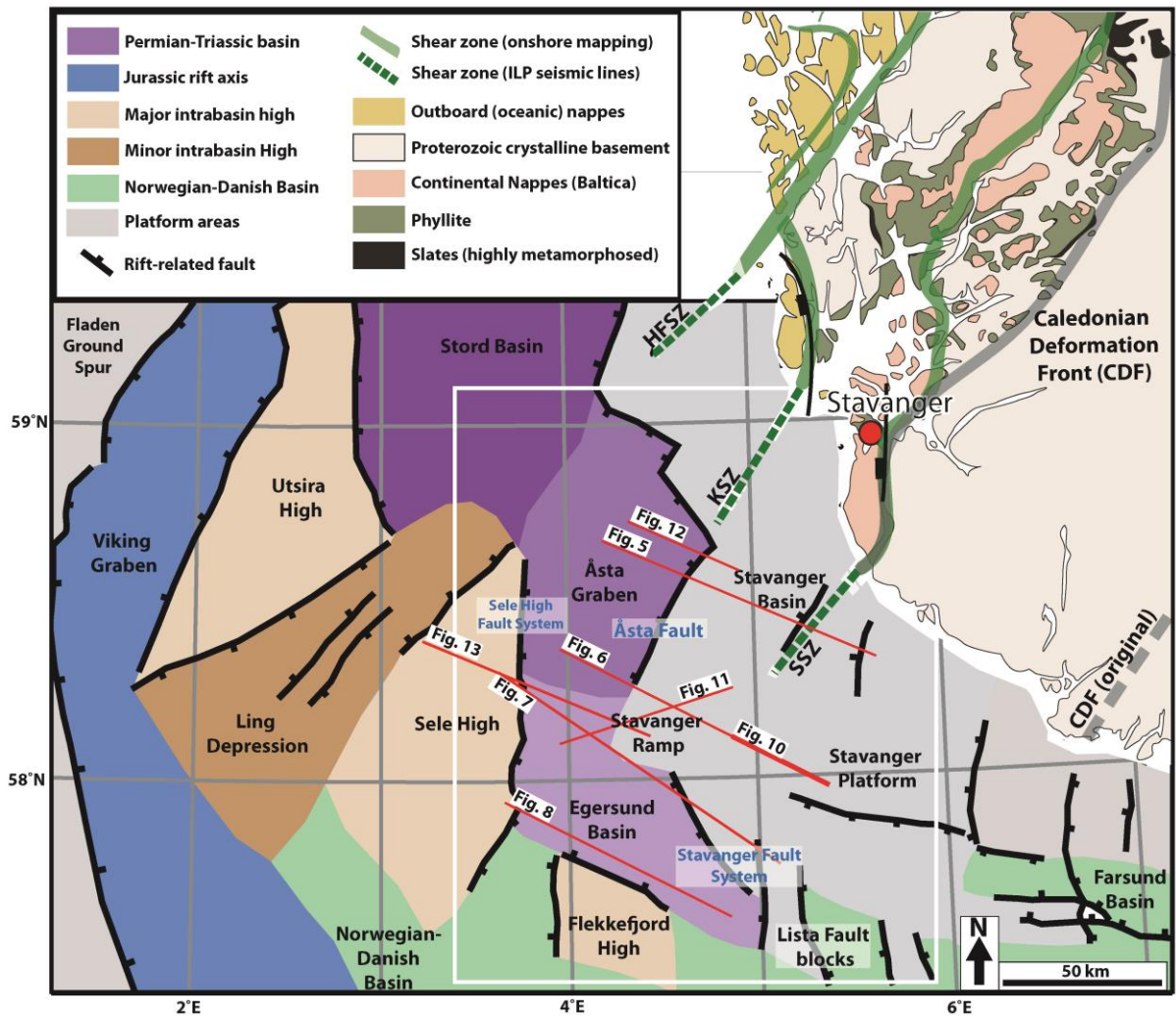
975

976

977

978

979 **Figure 1**



980

981

982

983

984

985

986

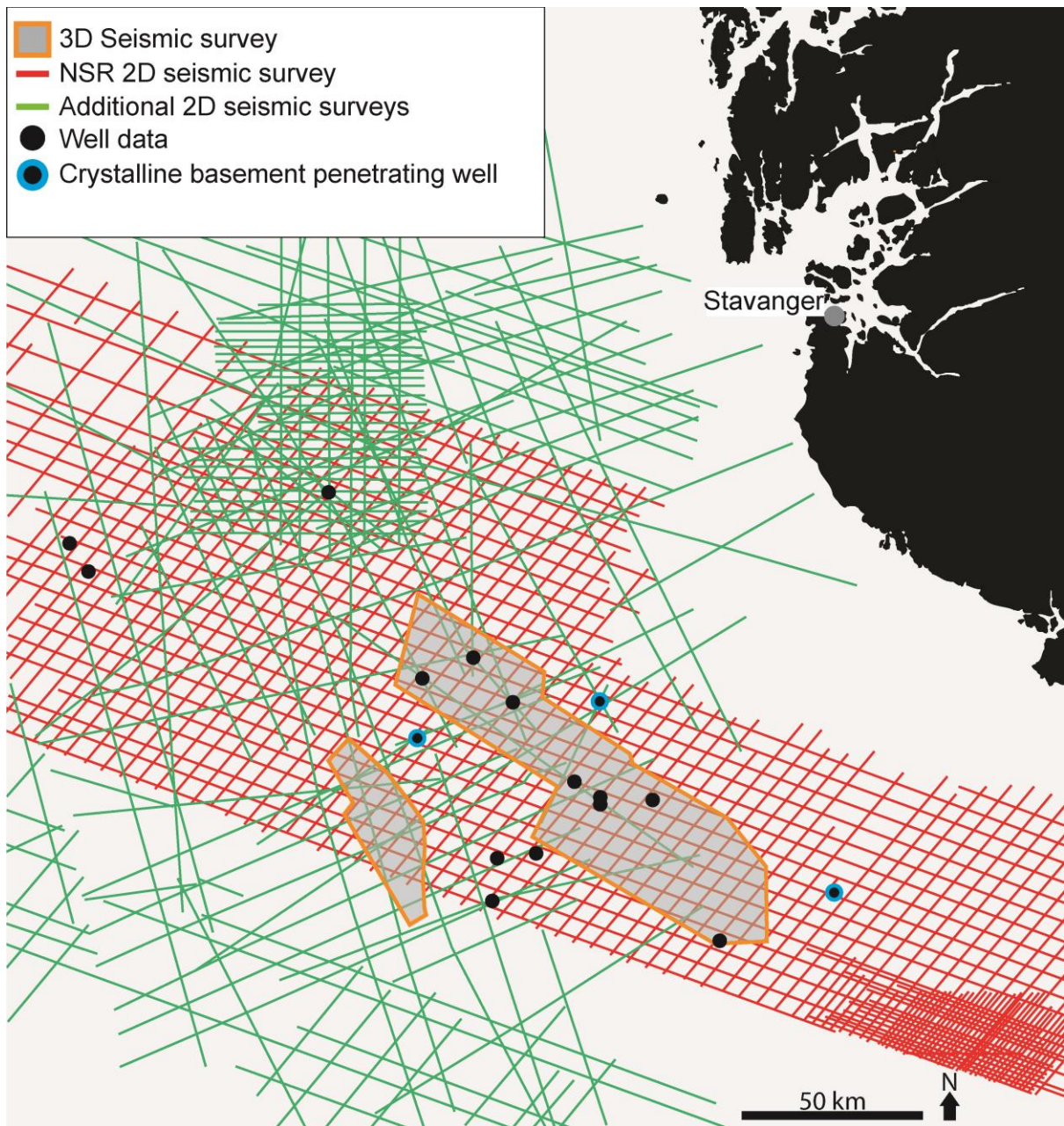
987

988

989

990

991 Figure 2



992

993

994

995

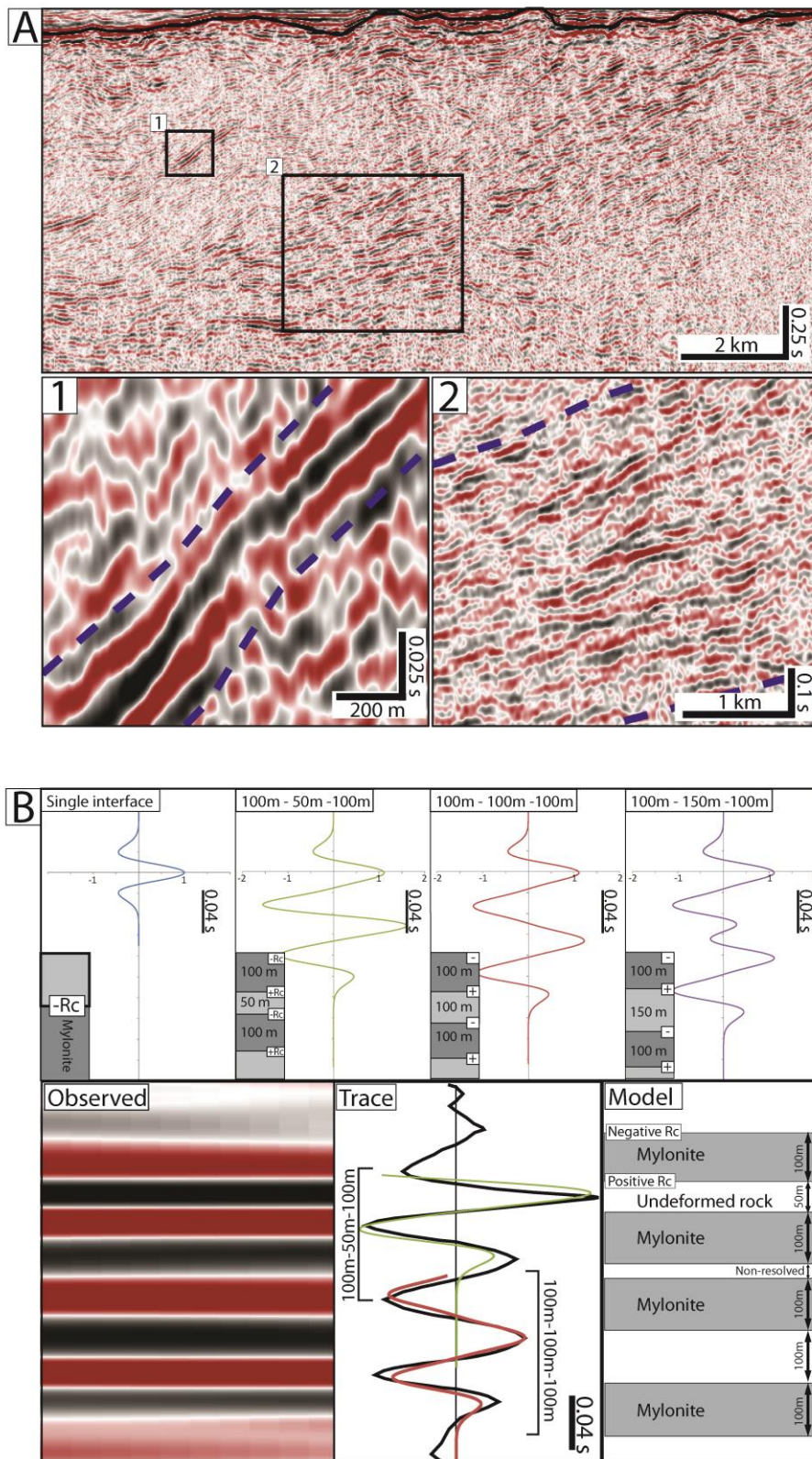
996

997

998

999

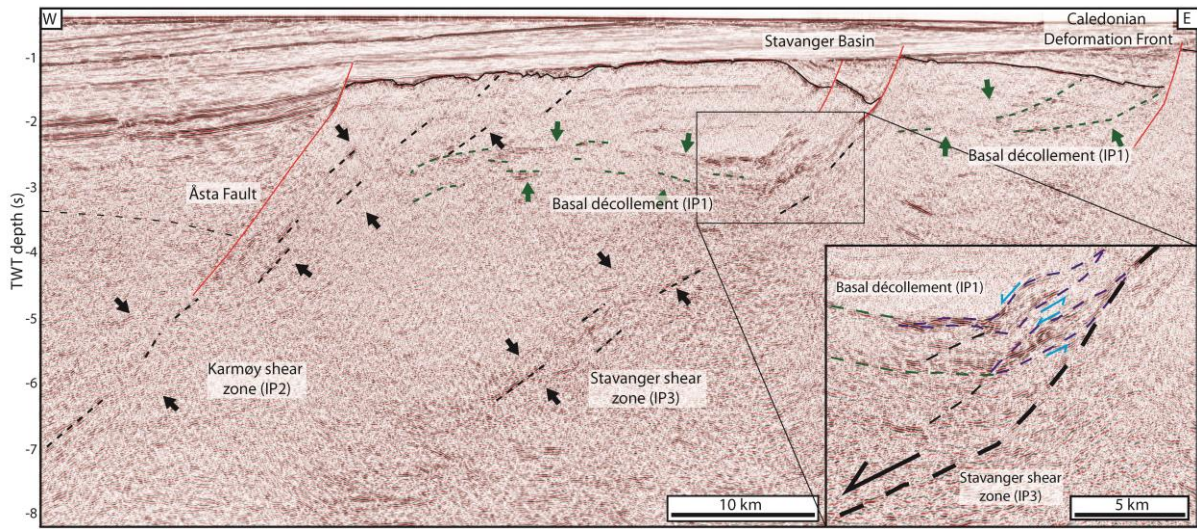
1026 Figure 4



1027

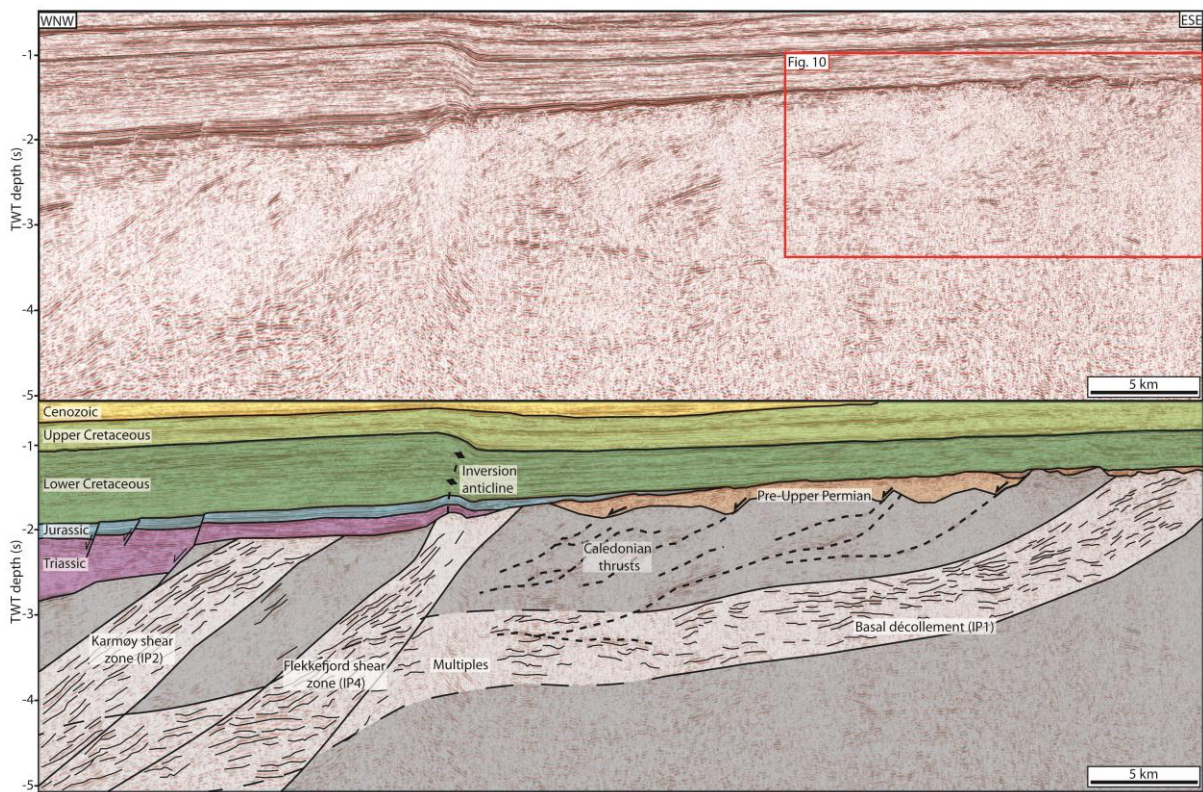
1028

1029 Figure 5



1030

1031 Figure 6



1032

1033

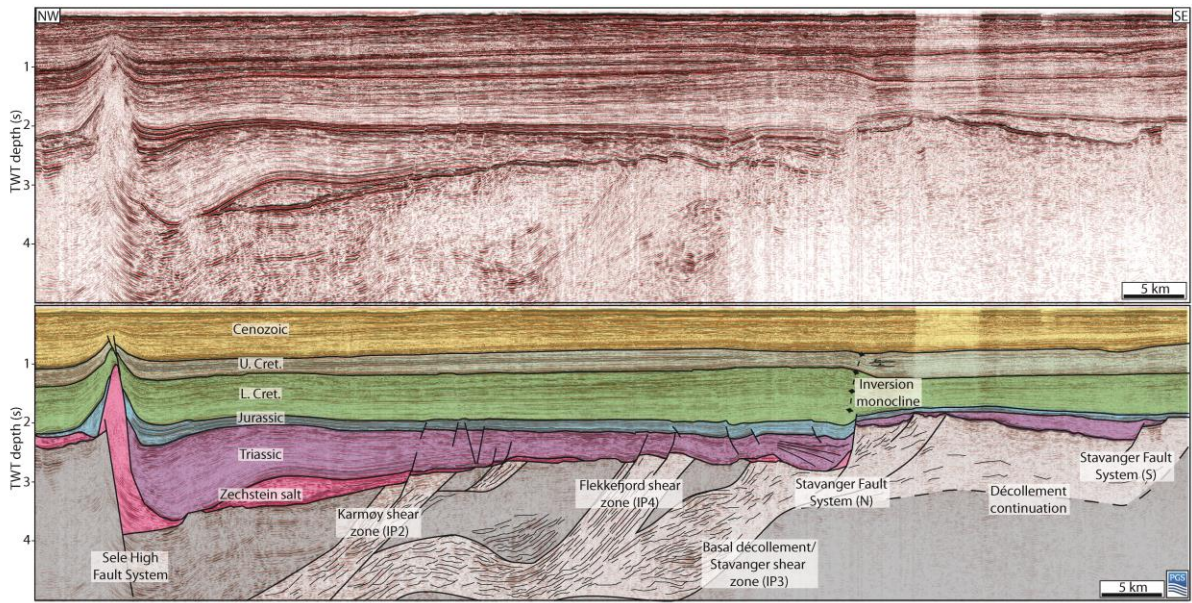
1034

1035

1036

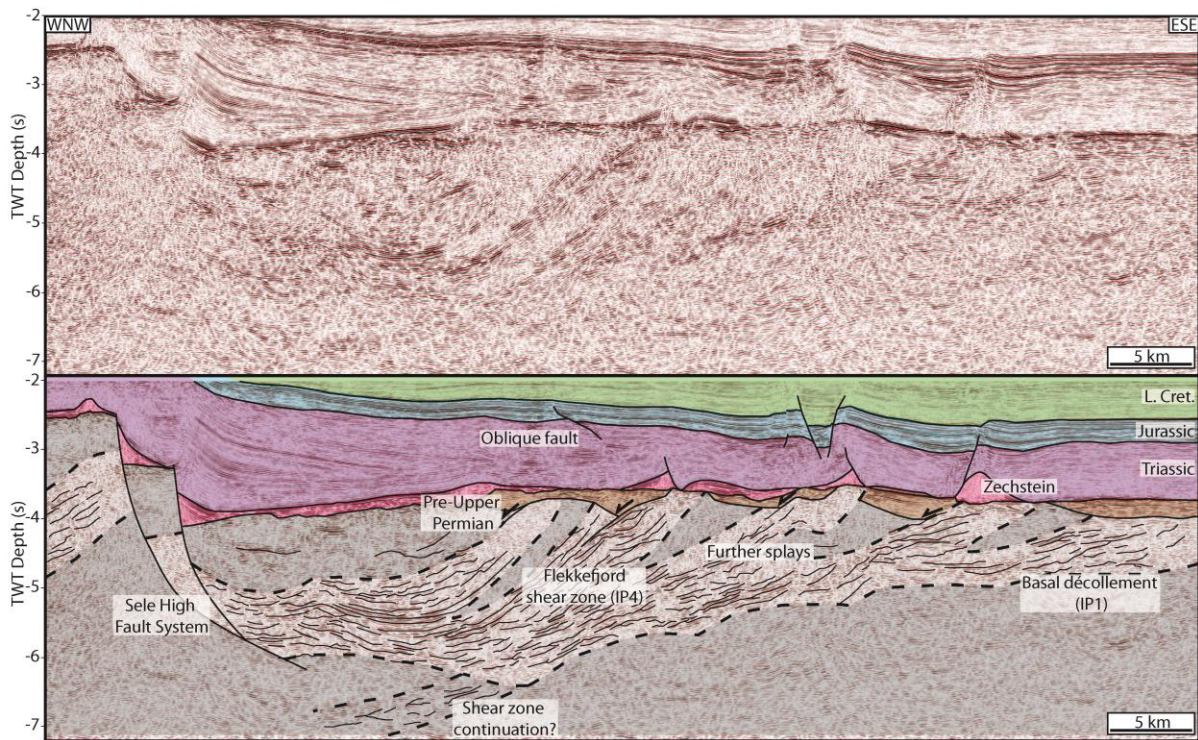
1037

1038 Figure 7



1039

1040 Figure 8



1041

1042

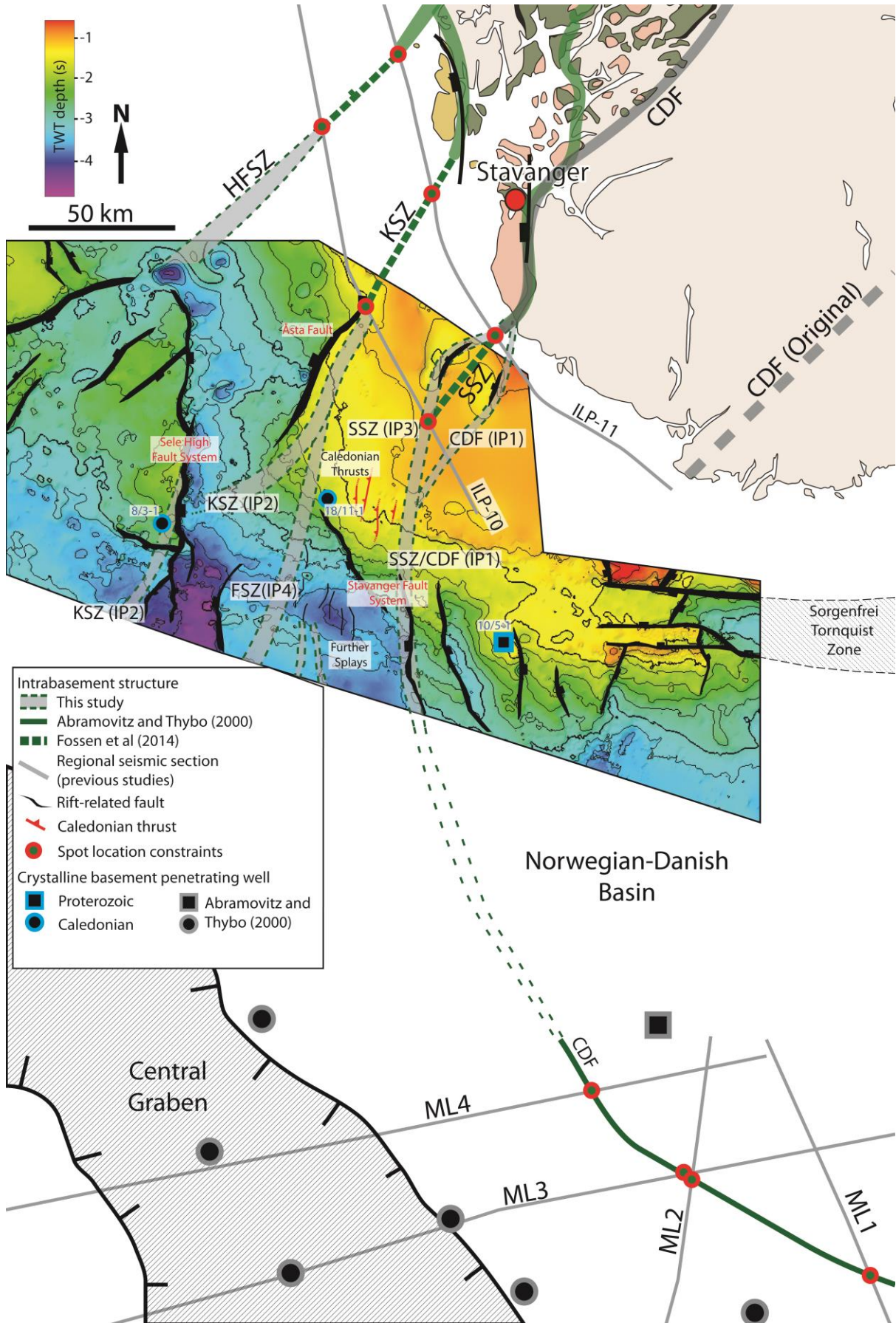
1043

1044

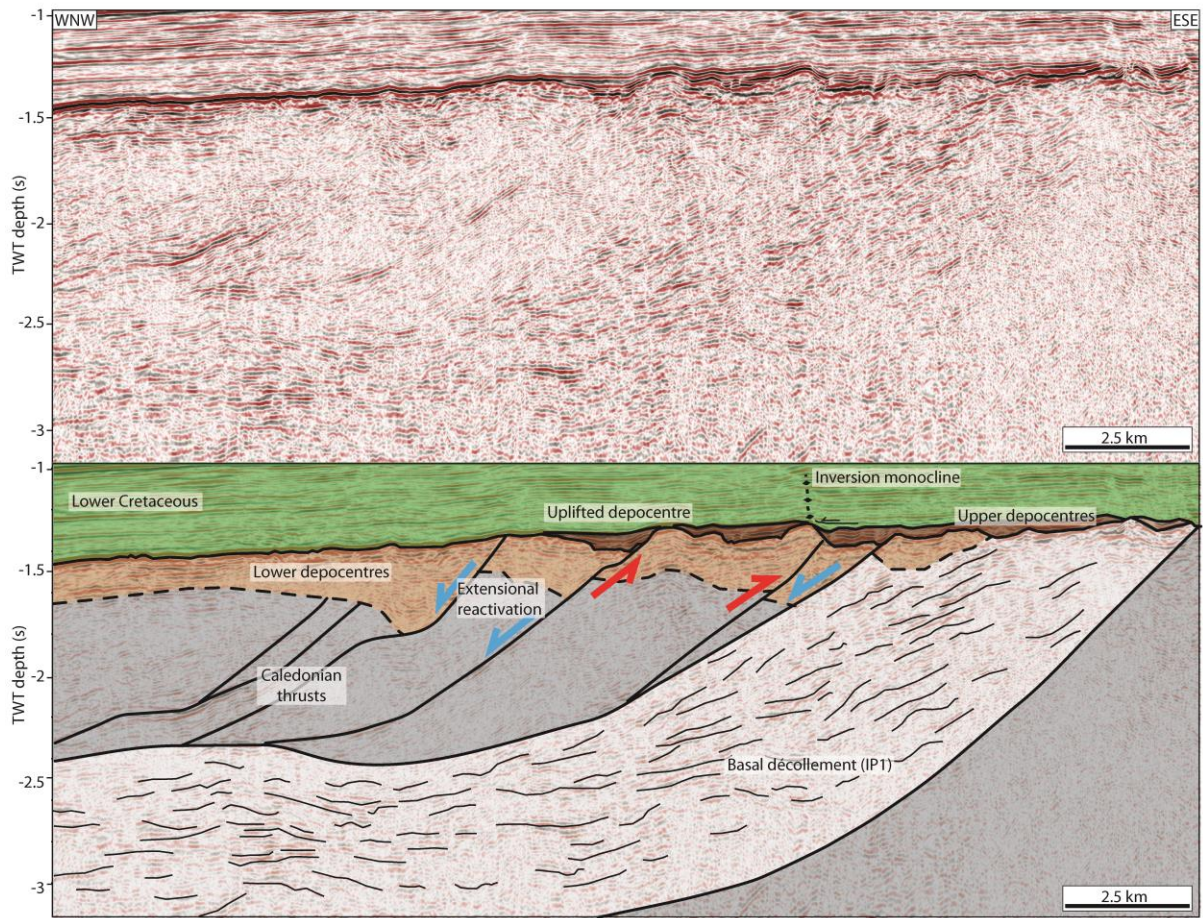
1045

1046

1047 Figure 9

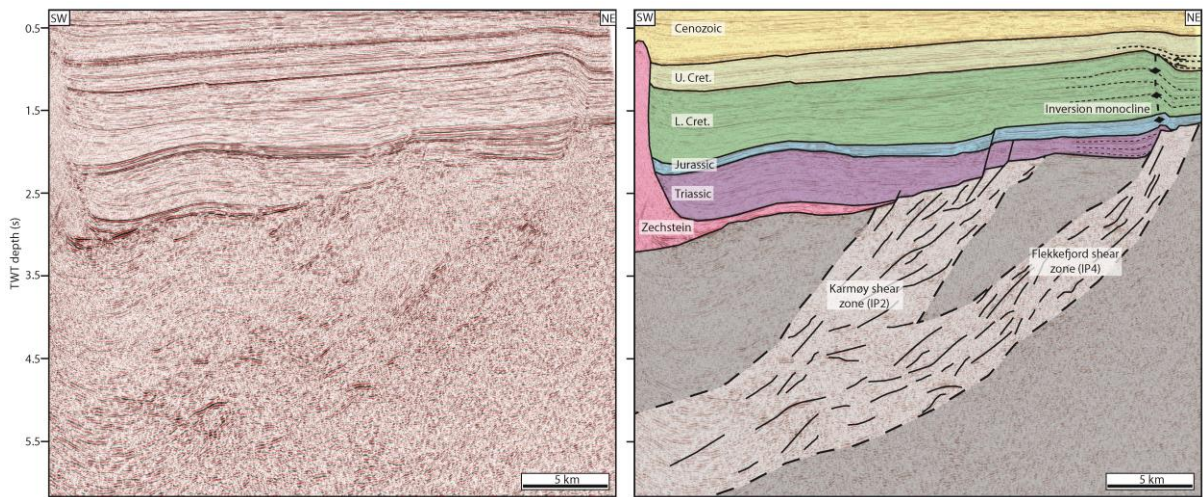


1049 Figure 10



1050

1051 Figure 11



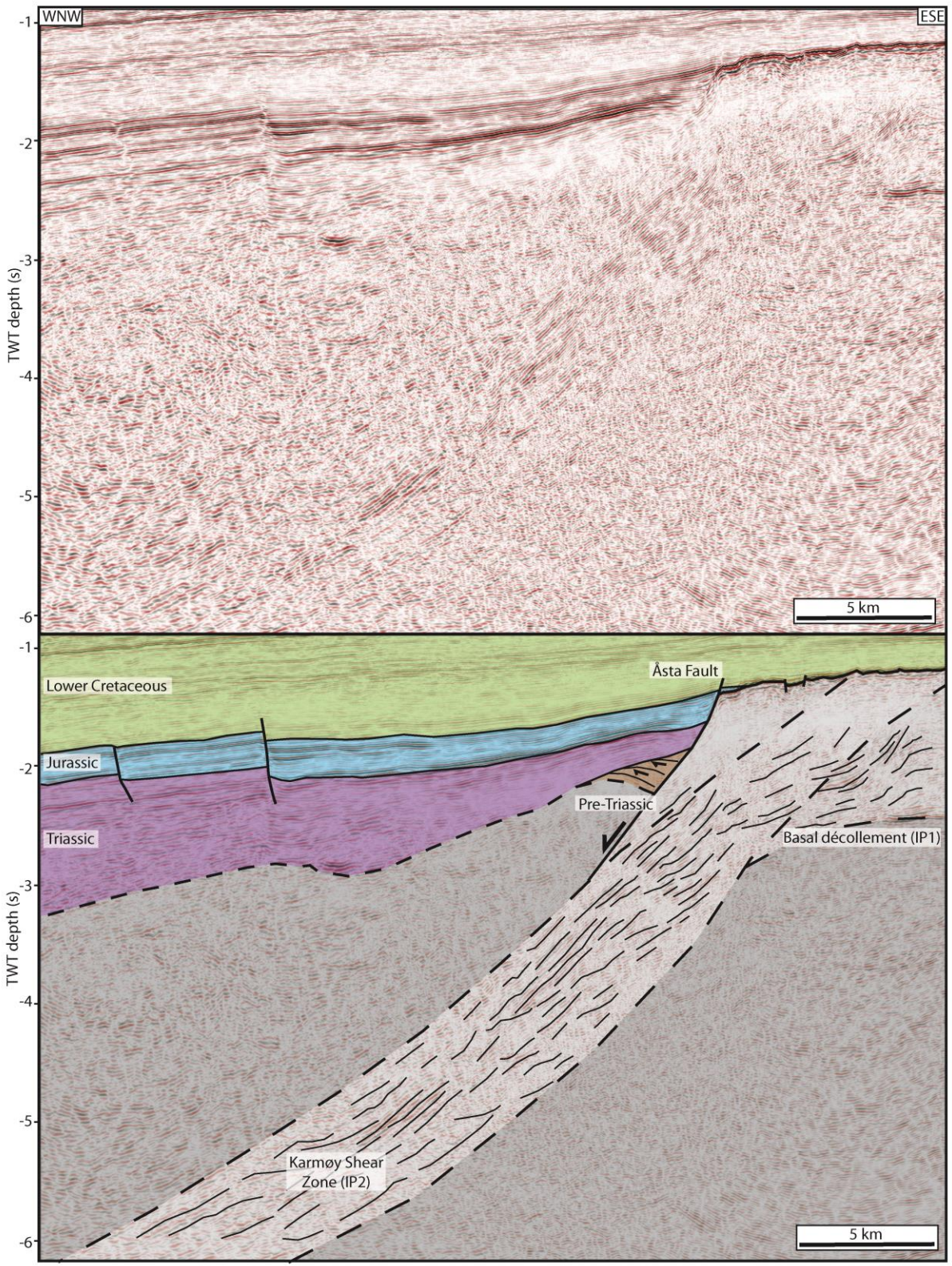
1052

1053

1054

1055

1056 Figure 12

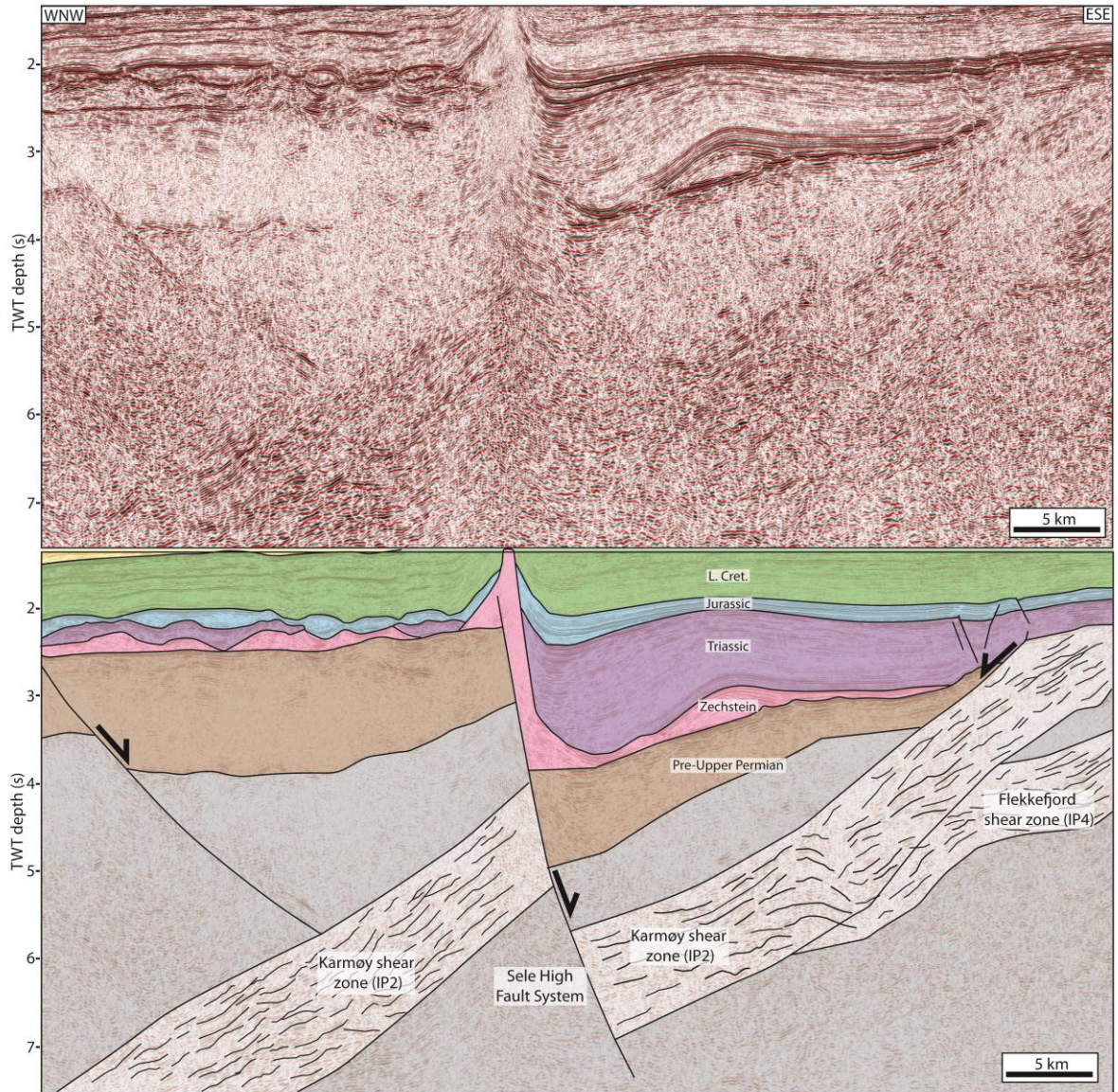


1057

1058

1059

1060 Figure 13



1061

1062

1063

1064

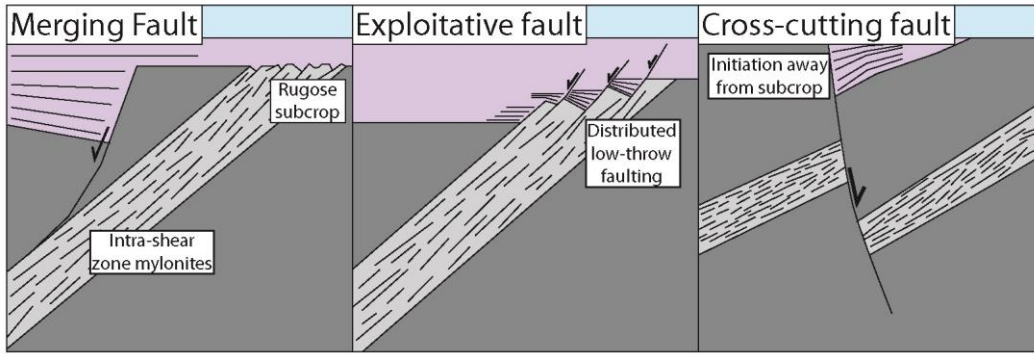
1065

1066

1067

1068

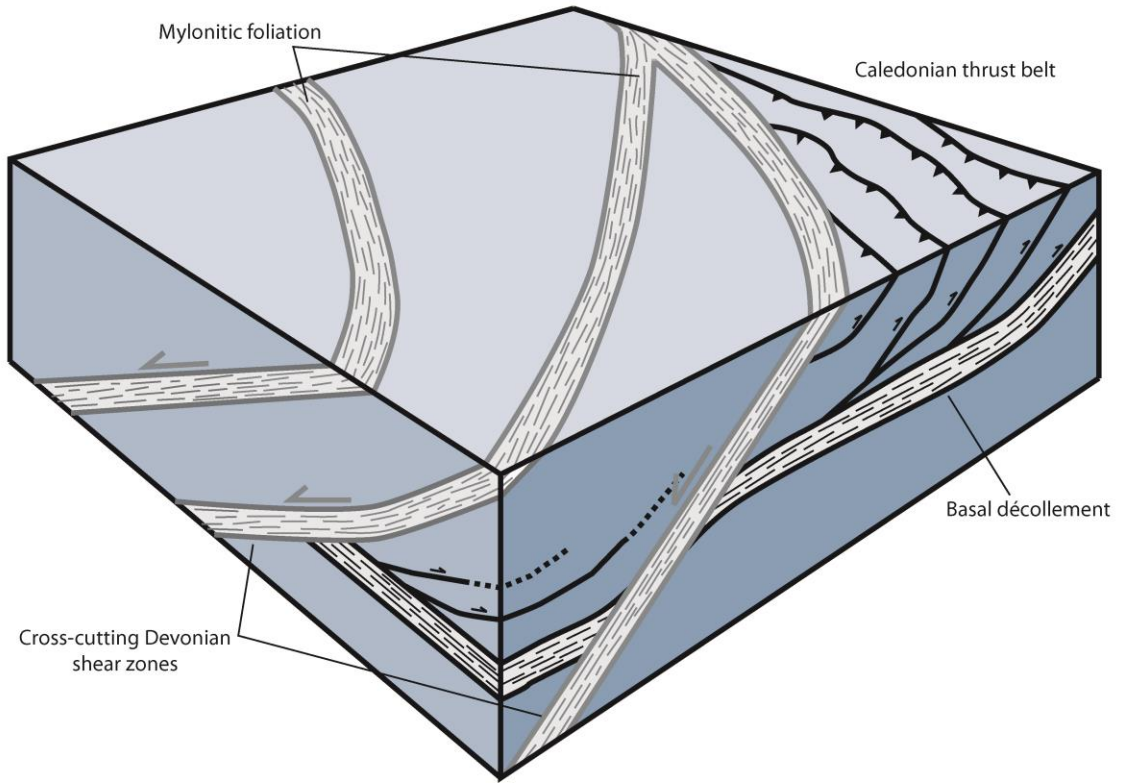
1069 Figure 14



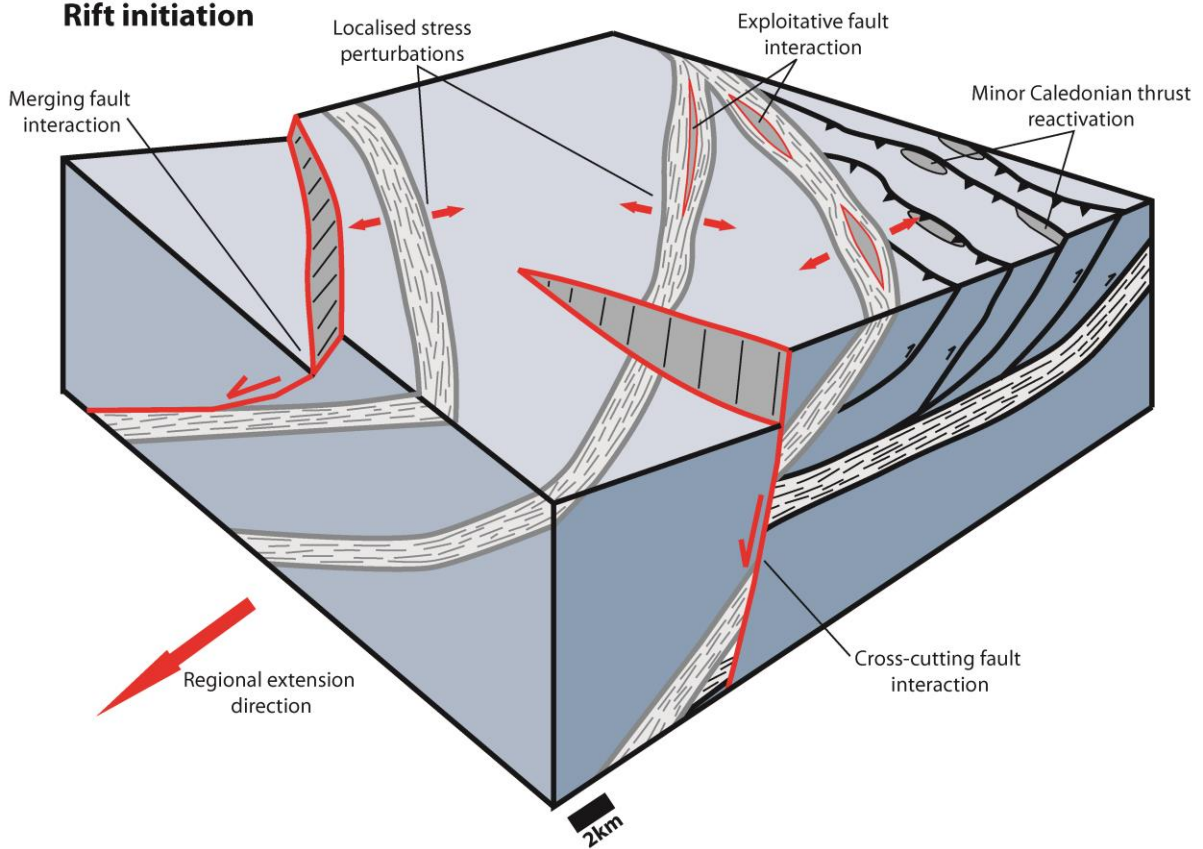
1070

1071 Figure 15

Pre-rift intrabasement structural framework



Rift initiation



1072

1073

1074